

1 **Wind Redistribution of Snow Impacts the Ka- and Ku-band Radar**
2 **Signatures of Arctic Sea Ice**

3 Vishnu Nandan^{1,2*}, Rosemary Willatt³, Robbie Mallett^{1,3}, Julianne Stroeve^{1,3}, Torsten Geldsetzer², Randall
4 Scharien⁴, Rasmus Tonboe⁵, John Yackel², Jack Landy⁶, David Clemens-Sewall⁷, Arttu Jutila⁸, David N.
5 Wagner^{9,10}, Daniela Krampe⁸, Marcus Huntemann¹¹, Mallik Mahmud², David Jensen¹, Thomas Newman³, Stefan
6 Hendricks⁸, Gunnar Spreen¹¹, Amy Macfarlane⁹, Martin Schneebeli⁹, James Mead¹², Robert Ricker¹³, Michael
7 Gallagher¹⁴, Claude Duguay^{15,16}, Ian Raphael⁷, Chris Polashenski⁷, Michel Tsamados³, Ilkka Matero⁸ and Mario
8 Hoppmann⁸.

9
10 ¹Centre for Earth Observation Science (CEOS), University of Manitoba, Canada

11 ²Department of Geography, University of Calgary, Canada

12 ³Centre for Polar Observation and Modeling, Earth Sciences, University College London, UK

13 ⁴Department of Geography, University of Victoria, Canada

14 ⁵DTU Space, Technical University of Denmark, Denmark

15 ⁶Centre for Integrated Remote Sensing and Forecasting for Arctic Operations (CIRFA), UiT The Arctic University of
16 Norway, Tromsø, Norway

17 ⁷Thayer School of Engineering, Dartmouth College, USA

18 ⁸Alfred Wegener Institute, Helmholtz Centre for Polar and Marine Research, Bremerhaven, Germany

19 ⁹WSL Institute for Snow and Avalanche Research (SLF), Davos, Switzerland

20 ¹⁰CRYOS, School of Architecture, Civil and Environmental Engineering, EPFL, Lausanne, Switzerland

21 ¹¹Institute of Environmental Physics, University of Bremen, Germany

22 ¹²ProSensing Inc, Amherst, MA, USA

23 ¹³Norce Norwegian Research Centre AS, Bergen, Norway

24 ¹⁴Physical Sciences Laboratory, NOAA, USA

25 ¹⁵Department of Geography and Environmental Management, University of Waterloo, Canada

26 ¹⁶H2O Geomatics Inc., Waterloo, Canada

27
28
29 *Correspondence: Vishnu Nandan (Vishnu.Nandan@umanitoba.ca)

30
31
32

33 **Abstract:** Wind-driven redistribution of snow on sea ice alters its topography and microstructure, yet the impact of these
34 processes on radar signatures is poorly understood. Here, we examine the effects of snow redistribution over Arctic sea ice
35 on radar waveforms and backscatter signatures obtained from a surface-based, fully-polarimetric Ka- and Ku-band radar, at
36 incidence angles between 0° (nadir) and 50°. Two wind events in November 2019 during the MOSAiC International Arctic
37 Drift Expedition are evaluated. During both events, changes in Ka- and Ku-band radar waveforms and backscatter coefficients
38 at nadir are observed, coincident with surface topography changes measured by a terrestrial laser scanner. At both frequencies,
39 redistribution caused snow densification at the surface and the uppermost layers, increasing the scattering at the air/snow
40 interface at nadir and its prevalence as the dominant radar scattering surface. The waveform data also detected the presence
41 of previous air/snow interfaces, buried beneath newly deposited snow. The additional scattering from previous air/snow
42 interfaces could therefore affect the range retrieved from Ka- and Ku-band satellite altimeters. With increasing incidence
43 angles, the relative scattering contribution of the air/snow interface decreases, and the snow/sea ice interface scattering
44 increases. Relative to pre-wind event conditions, azimuthally averaged backscatter at nadir during the wind events increases
45 by up to 8 dB (Ka-band) and 5 dB (Ku-band). Results show substantial backscatter variability within the scan area at all
46 incidence angles and polarizations, in response to increasing wind speed and changes in wind direction. Our results show that
47 snow redistribution and wind compaction need to be accounted to interpret airborne and satellite radar measurements of
48 snow-covered sea ice.

49

50

51

52

53

54

55

56

57

58

59

60

61

62 **1 Introduction**

63 Wind plays an important role in shaping the spatial distribution of snow depth and snow water equivalent (SWE) over sea ice
64 (Moon et al., 2019; Iacozza & Barber, 2010). Wind alters snow temperature gradients through wind pumping (Colbeck,
65 1989), structural anisotropy (Leinss et al., 2020), and snow grain geometry (Löwe et al., 2007). Furthermore, wind affects
66 the residence and sintering time of snow close to the surface, facilitating depositional snow dune growth and erosional
67 processes (Trujillo et al., 2016). Fluctuating wind speed and direction modify snow surface topography and density via wind
68 scouring and compaction of snow (Lacroix et al., 2009). Depending on the ice surface roughness (e.g., level ice, pressure
69 ridges, hummocks etc.), wind will result in the formation of heterogeneities at different scales, from ripple marks to snow
70 bedforms and drifts (Filhol & Sturm, 2015). This further alters the geometric, aerodynamic, and radar-scale roughness
71 (Savelyev et al., 2006).

72 Under cold snow conditions, a common assumption in radar altimetry is that the dominant scattering surfaces of co-polarized
73 Ka- and Ku-band radar signals correspond to the air/snow and snow/sea ice interfaces, respectively (e.g., Armitage et al.,
74 2015; Tilling et al., 2018). For synthetic aperture radar (SAR) and scatterometry, variations in snow grain microstructure
75 influence the proportion of surface and volume scattering to the total radar backscatter (Nandan et al., 2017). Winds can
76 roughen/smoothen the snow surface on relatively short time scales, altering the Ka- and Ku-band surface and/or volume
77 scattering contributions to total radar backscatter.

78 Very little is known about how wind redistribution of snow impacts snow depth, SWE, and ice thickness retrievals from
79 airborne and satellite radars (Yackel & Barber, 2007; Kurtz et al., 2009; Kurtz & Farrell, 2011). Due to repeat airborne and
80 satellite ground-tracks often occurring weeks/months apart and sea ice drift, it is challenging to measure radar backscatter
81 changes resulting from wind redistribution, on the same area of ice over time. Nevertheless, Kurtz & Farrell (2011) assumed
82 snow redistribution caused an anomalous snow depth decrease in 2009 over multi-year sea ice in the Canadian Archipelago
83 (CA), retrieved from two Operation IceBridge (OIB) snow radar flights, acquired three weeks apart. Yackel & Barber (2007)
84 speculated that snow redistribution on first-year sea ice in the CA was, in part, responsible for a change in retrieved SWE of
85 up to 7 cm, derived from two C-band RADARSAT-1 images 45 days apart.

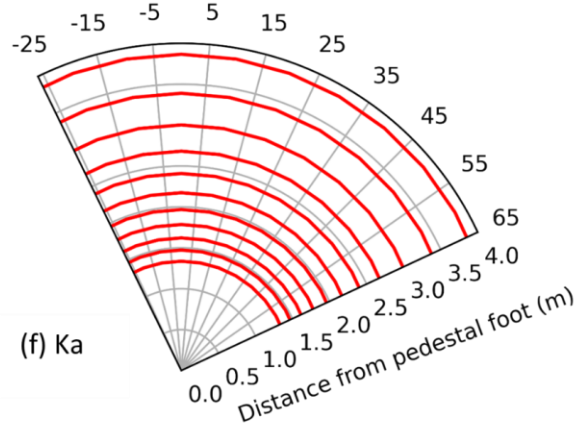
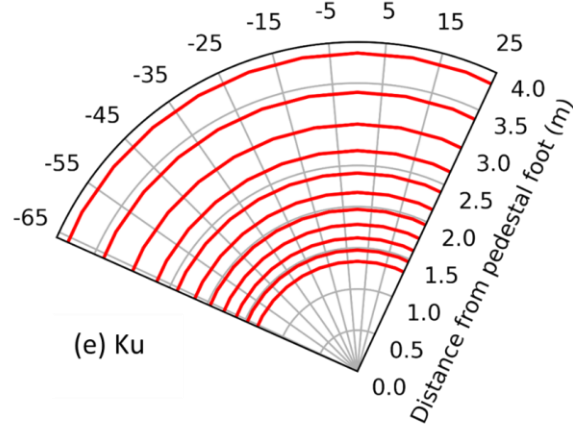
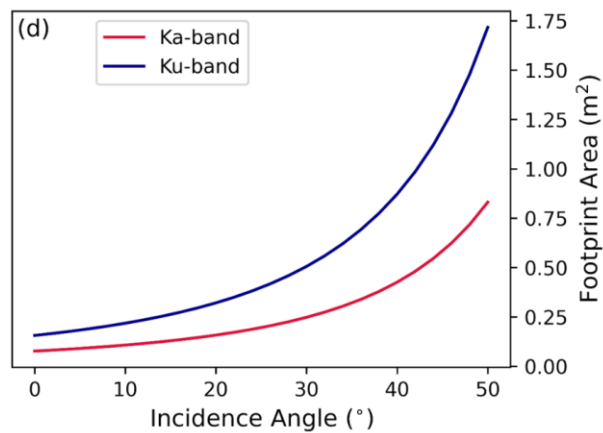
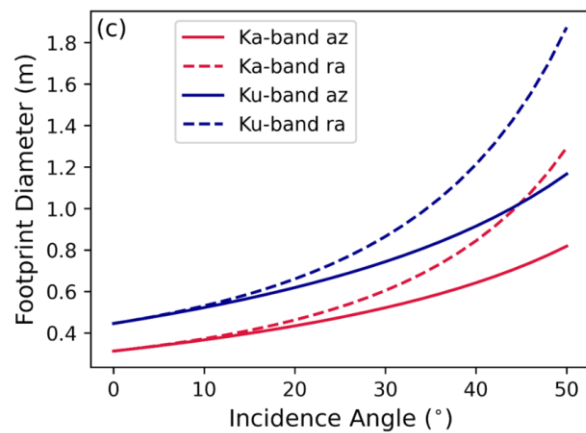
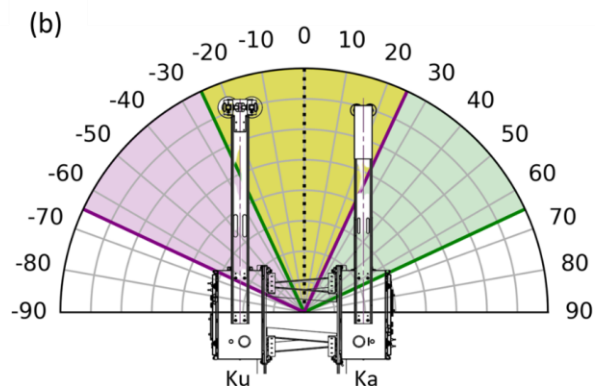
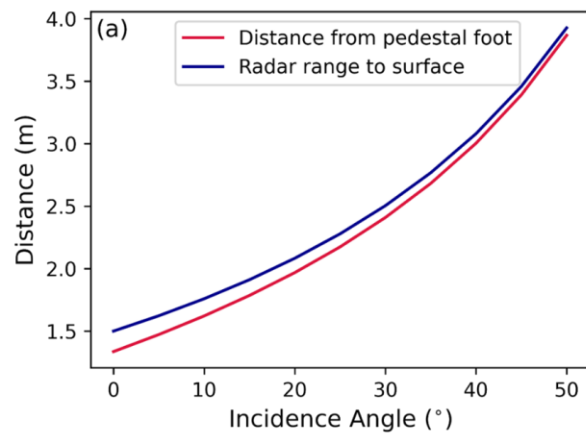
86 To better understand the impact of snow redistribution on Ka- and Ku-band radar signatures, we require unambiguous in-situ
87 measurements of snow physical properties and meteorological observations during wind events, sampled coincidentally with
88 radar measurements. This bridges a fundamental knowledge gap, and potentially allows improved modelling of Ka- and Ku-
89 band radar waveforms and backscatter. This in turn may improve interpretation of Ka- and Ku-band radar signatures from
90 presently operational SARAL/AltiKa (Guerreiro et al., 2016), CryoSat-2 (Lawrence et al., 2018), Sentinel-3 (Lawrence et al.,
91 2021), ScatSat-1 (Singh & Singh, 2020) and the upcoming Ka-/Ku-band CRISTAL altimetry (Kern et al., 2020) and SWOT
92 satellite missions (Armitage & Kwok, 2021).

94 In this study, we investigate wind-induced changes to snow physical properties and topography on Ka- and Ku-band radar
95 signatures including dominant scattering surfaces and backscatter using a surface-based, fully-polarimetric, Ku- and Ka-band
96 radar (KuKa radar; see Stroeve et al., 2020) deployed during the 2019-20 Multidisciplinary drifting Observatory for the Study
97 of Arctic Climate (MOSAiC) expedition (Nicolaus et al., 2022). We present data from 9 to 16 November 2019, assessing the
98 effects of two separate Wind Events (WE1 and WE2). First, we describe the KuKa radar system, the time series of
99 meteorological observations, snow physical properties, and snow surface topography. Next, we investigate the impact of
100 snow redistribution on KuKa radar echograms and waveforms, examining changes in dominant scattering surfaces and radar
101 backscatter. Finally, we discuss the relevance of our findings to improving retrievals of snow/sea ice geophysical variables
102 by airborne and satellite radars.

103 **2. Data and Methods**

104 **2.1 Surface-Based Ka- and Ku-band Polarimetric Radar (KuKa Radar)**

105 During the MOSAiC expedition, the research icebreaker *R/V Polarstern* drifted with a sea ice floe across the central Arctic
106 Ocean over a full annual cycle (Nicolaus et al., 2022). The floe was dominated by second-year ice with refrozen melt ponds
107 making up ~ 60% of the surface area. The Remote Sensing Site (RSS) was first established on the floe on 18 October 2019,
108 where the KuKa radar was deployed on ~ 80 cm thick, laterally homogeneous, and undeformed sea ice.



110 Figure 1: KuKa radar geometry illustrating (a) radial distance and radar range from the pedestal foot; (b) KuKa radar

111 azimuth scan pattern projected based on the positioner axis coordinate system (b) scan pattern of radar projected onto a level
112 surface; (c) diameter of radar scan area, measured radially ('ra') and azimuthally ('az'); (d) area of radar scan area; (e) and
113 (f) Ku- and Ka-band scan area of the KuKa radar, respectively. In panel (b), the region between purple and green lines are
114 the respective Ku- and Ka-band scan area (separately illustrated in panels (e) and (f), while the yellow region in (b) is the
115 overlapping scan area.

116 The KuKa radar transmits at Ka- (30-40 GHz) and Ku-band (12-18 GHz) frequencies and measures the return radar power (in
117 dB) as a function of range (Stroeve et al. 2020). The radar acquires data across a fixed azimuth (θ_{az}) range, at discrete incidence
118 angle (θ_{inc}) intervals. The radar operates in all vertical (V) and horizontal (H) linear polarization transmit and receive
119 combinations: VV, HH, HV, and VH.

120 The central frequency of the radar chirps were set to be close to the Ka-band of AltiKa (35 GHz) and the Ku-band of CryoSat-
121 2 (13.575 GHz). The KuKa radar bandwidth is considerably higher than the bandwidth of AltiKa and CryoSat-2, allowing
122 improved range resolution of 1.5 cm for Ka-band and 2.5 cm for Ku-band relative to 30 cm and 46 cm for AltiKa and CryoSat-
123 2, respectively. The radial distance and range from the pedestal, the scan area diameter, and scan area from $\theta_{inc} = 0^\circ - 50^\circ$ are
124 illustrated in Figure 1. During MOSAiC, the KuKa radar scanned over a 90° continuous θ_{az} range width for every 5° interval
125 in θ_{inc} . The KuKa radar takes ~ 16 seconds (i.e., 5.7° per second) over a 90° θ_{az} width to acquire data across an incidence
126 angle scan line and ~ 2.5 minutes for one complete scan between $\theta_{inc} = 0^\circ - 50^\circ$. There is a $\sim 20^\circ$ offset between the individual
127 radar antennas and the radar positioner axis origin. Therefore, the Ku-band antenna scans between -65° to $+25^\circ$ θ_{az} range
128 (region between purple lines) from -25° to $+65^\circ$ for Ka-band (region between green lines) (Figure 1(b), (e) and (f)). This also
129 means that the Ku- and Ka-band scan area overlap for a given radar 'shot' is θ_{inc} dependent. The yellow region between green
130 and purple lines in Figure 1b between -25° and $+25^\circ$ is the overlapping Ku- and Ka-band scan area. The antenna beamwidth
131 (6 dB two-way) is 16.9° and 11.9° for Ku- and Ka- bands, respectively. Therefore, the size of the radar scan area on the snow
132 is dependent on frequency, height of the antenna above the snow surface, and θ_{inc} . Further description of the radar
133 specifications, signal processing, polarimetric calibration routine, signal-to-noise and error estimation is documented in
134 Stroeve et al. (2020).

135 At the RSS, the radar acquired scans every 30 mins over the 90° θ_{az} width and θ_{inc} discrete increments. Between 9 and 15
136 November, a total of 325 scans were collected. The ice supporting the RSS broke up on 16 November, and the measurements
137 were stopped until it was safe to redeploy the radar.

138

139 **2.2 Meteorological and Snow Property Data**

140 A 10-m tall meteorological station installed ~ 100 m away from the RSS monitored air temperature (°C), relative humidity
141 (%)
142 (hPa), wind speed (m/s) and wind direction (°), all at 2 m height. Wind direction is denoted with respect to
143 geographic north (0°). Measurements were acquired every second (Cox et al., 2021) and resampled to 30-minute averages, to
match the radar scan intervals.

144 A thermal infrared (TIR) camera (Infratec VarioCam HDx head 625, assuming emissivity 0.97 at 7.5-14 μ m wavelength;
145 Spreen et al., 2022) measured snow surface temperature (°C), every 10 minutes. Two digital thermistor chains (DTC) installed
146 close to the RSS measured near-surface, snow, and sea ice temperature evolution at 2 cm vertical intervals. No destructive
147 snow sampling was done underneath the KuKa radar scan area. Instead, snow depth measurements were made close to the
148 radar on 4 and 14 November. Profiles of the penetration resistance force of the snow were collected before, during and after
149 WE1 and WE2 using a Snow Micro penetrometer (SMP; Johnson & Schneebeli, 1999) at the Snow1, Snow2 and the RSS sites
150 (see locations in Figure 4). Five SMP profiles per pit were recorded weekly. To compare initial density and SSA between the
151 RSS and the Snow1 and Snow2 locations at the beginning of November, one SMP profile from the RSS was taken on 4
152 November. The force profiles were converted into density and specific surface area (SSA) following King et al. (2020) and
153 Proksch et al. (2015) parameterizations, respectively, that also worked well during the MOSAiC winter (Wagner et al., 2022).

154 **2.3 Snow Surface Topography**

155 An optical camera was used to visualise snow surface topography changes within the radar scan area (Spreen et al., 2021). In
156 addition, Terrestrial Laser Scanning (TLS) data of snow surface topography were collected on 1, 8 and 15 November using a
157 Riegl VZ1000. Scan positions were registered in RiSCAN (Riegl's data processing software) using reflectors permanently
158 frozen to the ice and levelled based on the VZ1000's built-in inclination sensor. Wind-blown snow particles were removed
159 from the data by FlakeOut filtering (Clemens-Sewall et al., 2022). Filtered data were aligned to one another by matching
160 reflectors and other tie-points. To transform the TLS data into the KuKa radar's reference frame, the outlines of the radar's
161 pedestal column and the antenna arms were manually picked in the TLS data.

162
163 A non-linear least squares optimization method using SciPy (Virtannen et al 2020) was then implemented to estimate the best
164 fitting circle and rectangle to match the pedestal column and the antenna arms, respectively. The centre of the pedestal was
165 used as the horizontal origin, the centre of the antennas was used for orientation, and the antenna height at nadir position was
166 used as the vertical origin. Within the radar's reference frame, a polar grid was defined with radial increments of 0.25 m and
167 azimuthal increments of 10°. The surface height in the radar reference frame (a.k.a. the vertical distance from the surface to
168 the radar antennas at nadir) for each grid cell was calculated by averaging the vertical position of each TLS point within that
169 grid cell.

170 **2.5 Radar Waveforms and Backscatter**

171 Waveforms from each sampling time across θ_{az} were recorded and overlaid with the TLS data to identify where the Ka- and
172 Ku-band backscatter originated from (Section 3.2). Deconvolved waveforms were used (Stroeve et al., 2020), using waveforms
173 from a refrozen lead located close to the RSS in January 2020 to provide a specular return useful for reducing the appearance
174 of sidelobes that result from non-ideal behaviour of the RF electronics, as well as internal reflections in the radar. Waveform
175 echograms were used to illustrate how the return waveforms from within the overlapping scan area changed between WE1
176 and WE2. The normalized radar cross section per unit area (NRCS) was calculated based on the range-power profiles following
177 the standard beam-limited radar range equation (Ulaby et al., 2014), given by:

178

$$NRCS = \frac{8\ln(2)h^2\sigma_c}{\pi R_c^4 \theta_{3dB}^2 \cos \theta} \left(\frac{\tilde{P}_r}{\tilde{P}_{rc}} \right)$$

179 where h is the antenna height, R_c is the range to the corner reflector, θ_{3dB} is the one-way half-power beamwidth of the antenna
180 and \tilde{P}_r and \tilde{P}_{rc} are the received power from the snow and the corner reflector, respectively.

181 The peak power in the radar waveforms used for calculating NRCS is determined by locating the highest peak in the waveform
182 averaged across all polarisations. For waveform analysis, we calculated NRCS at nadir for the air/snow and snow/ice interfaces
183 by integrating the power over the waveform peaks within +/- 2 dB either side from the overlapping scan area (Section 3.2).
184 Next, we calculated the NRCS value integrated over the entire snow volume based on the power contained within this peak
185 over an incidence angle scan line, by integrating over the range bins where the power falls below a threshold, set to -50 dB on
186 either side of the peak for Ka-band data, and -20 dB (-40 dB) on the on the smaller-range (larger-range) sides for Ku-band
187 data. The NRCS was averaged across the overlapping scan area across the entire 90° θ_{az} range, at discrete $\theta_{inc} = 0^\circ, 15^\circ, 35^\circ$
188 and 50°, to demonstrate scan area-scale variability in backscatter during the two wind events (section 3.3).

189 To investigate the sub-scan area scale backscatter variability caused by surface heterogeneity, as well as the range to the
190 dominant scattering surface that could have changed during sampling, we used azimuth ‘sectoring’ and analysed the NRCS
191 averaged at 5° wide θ_{az} bins. Azimuth ‘sectoring’ has an impact on the number of independent samples in range along a 5°
192 θ_{az} bin, since a smaller area is used for averaging (Table 1). The number of independent samples is estimated based on the
193 following steps: a) determine the distance between the 6 dB points below the radar range peak on either side of the peak, b)
194 divide the 6 dB range by the range resolution. This is a measure of the number of independent samples in range, c) divide the
195 azimuth width (90° and 5° in our study) by the azimuth beamwidth and multiply by 2, and d) the total number of independent
196 samples would then be the number of independent samples in range multiplied by the number of independent samples in
197 azimuth (Doviak & Zrnić, 1984).

198

199 **Table 1:** Number of independent samples at Ka- and Ku-band frequencies at nadir and $\theta_{inc} = 50^\circ$ at $\theta_{az} = 90^\circ$ and along a 5°
 200 bin

Frequency	Nadir		$\theta_{inc} = 50^\circ$	
	$\theta_{az} = 90^\circ$	$\theta_{az} = 5^\circ$	$\theta_{az} = 90^\circ$	$\theta_{az} = 5^\circ$
Ka-band	487	48	1609	439
Ku-band	198	34	1252	376

201

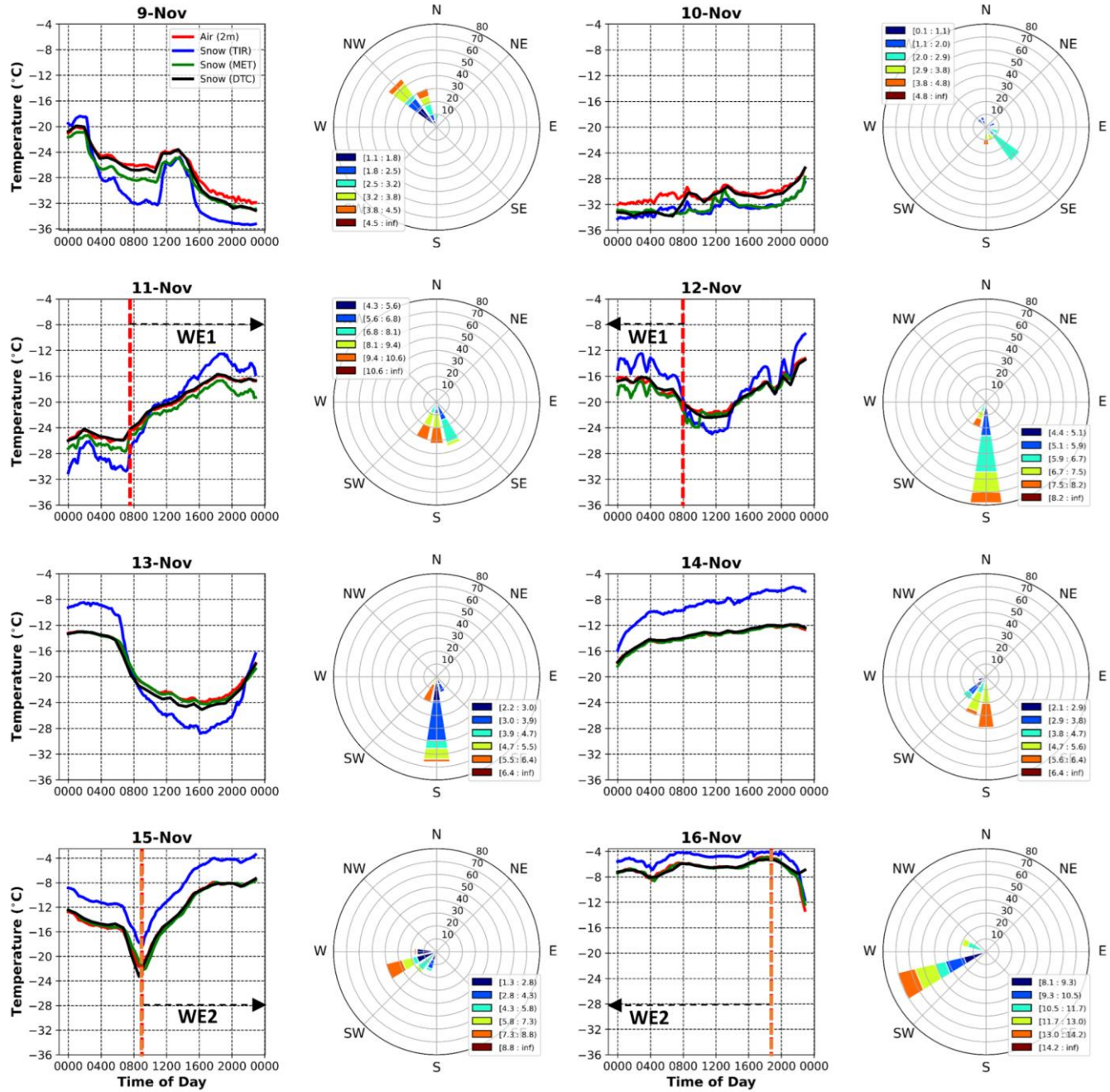
202 Within every θ_{inc} scan, VV, HH and HV are derived from the complex covariance matrix, while VH is discarded based on
 203 reciprocity of cross-polarized channels (i.e., HV \sim VH) (Ulaby et al., 2014). In Section 3.3.2, we show the changes in
 204 backscatter signature variability across the KuKa radar scan area at 5° wide θ_{az} bins at specific times on 9, 11 and 15
 205 November.

206 **3. Results**

207 **3.1 Meteorological and Snow Conditions**

208 **3.1.1 WE1 and WE2**

209 WE1 started \sim 0745 UTC on 11 November and lasted until \sim 0800 UTC on 12 November when winds \sim 12 m/s originated from
 210 the SW to SE (Figure 2 and 3c). WE2 started \sim 0900 UTC on 15 November, when a low-pressure system began to intensify
 211 (Figure 3b). The wind direction shifted from SW to W, and speeds increased to \sim 15 m/s and continued until \sim 1900 UTC on
 212 16 November (Figure 2 and 3c). During WE2, the strong low-pressure system dropped below 995 hPa (Figure 3d) and the air
 213 temperature reached -5.5°C (Figure 3a). The warm air advection was accompanied by a steep increase in relative humidity to
 214 $> 90\%$ (Figure 3d).



215

216 Figure 2: Line plots illustrate daily, 30-min averages of 2 m air temperature (MET tower) and snow surface temperature measurements
 217 from the TIR camera, MET tower and DTC sensors; acquired between 9 and 16 November. Wind speed (m/s) and direction (°) measurements recorded by the MET tower. All times are UTC. Dotted red and orange lines indicate the onset
 218 of WE1 and WE2, respectively, supported by black arrows.
 219

3.1.2 Snow Temperature, Density and Microstructure

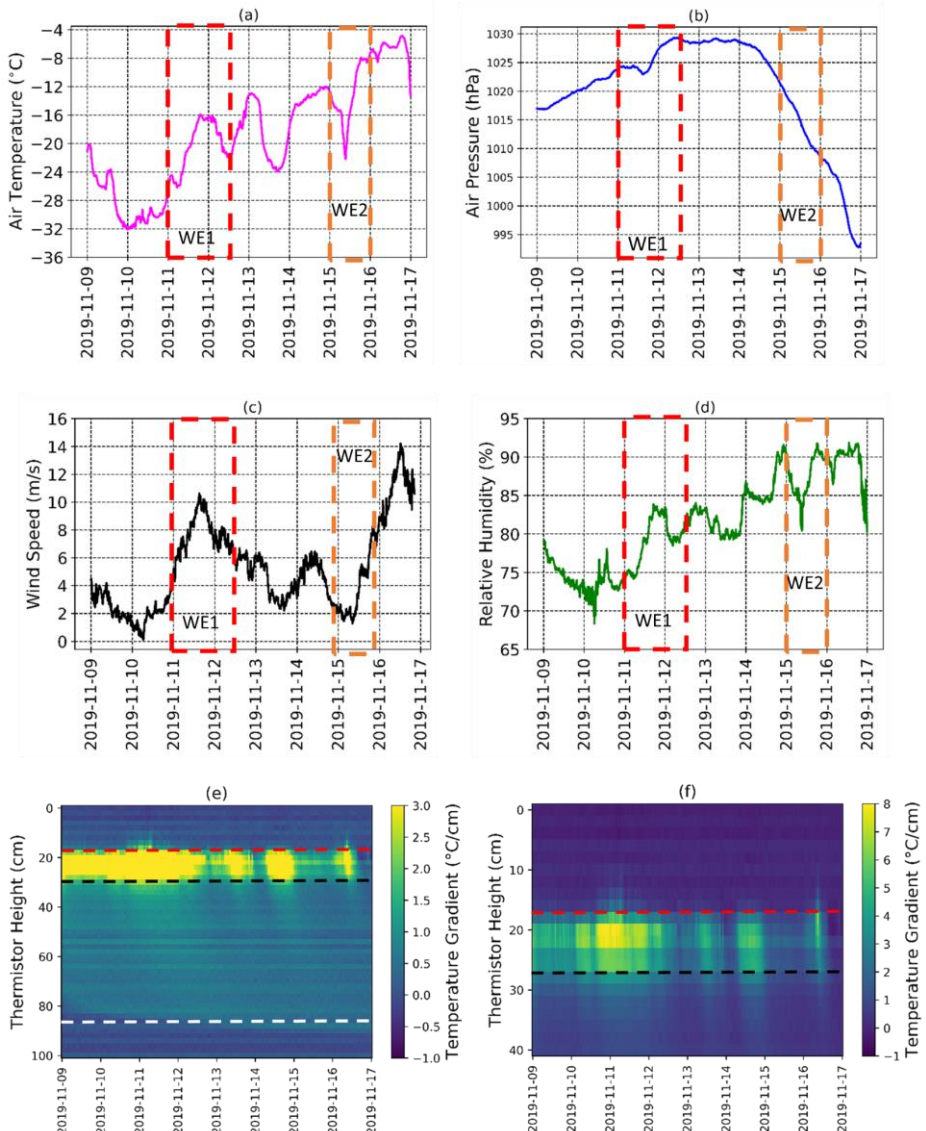
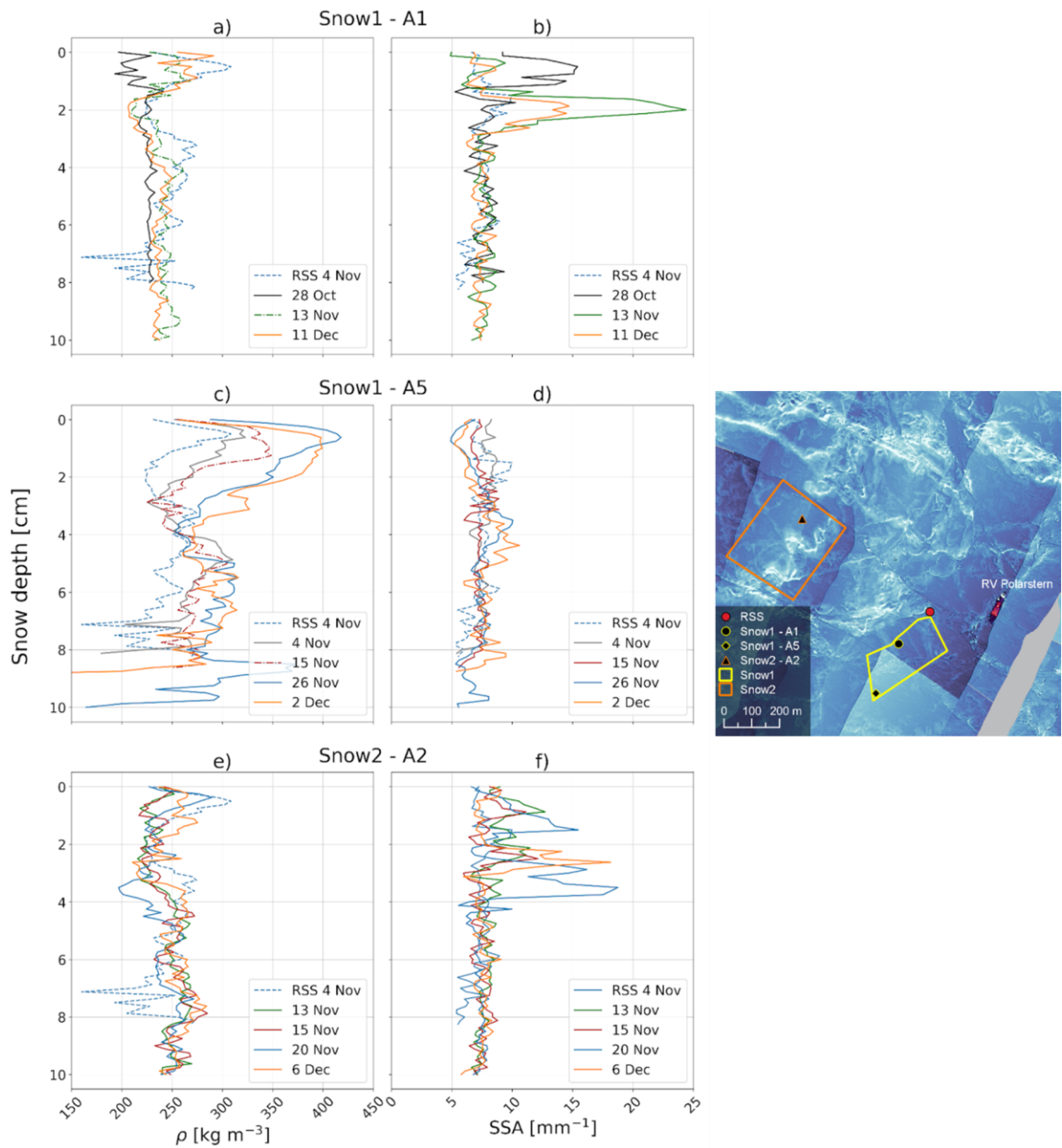


Figure 3: Line plots show daily, 10-min averaged 2m (a) air temperature, (b) air pressure, (c) wind speed and (d) relative humidity, recorded by the MET tower between 9 and 16 November. 2D color plots show DTC-derived hourly-averaged temperature gradient of (e) near-surface, snow, sea ice and ocean; and (f) sub-section of panel (e) showing the snow volume from the RSS. Yellow represents larger temperature gradients within the snowpack. Dotted red, black and white lines represent approximate locations of the estimated air/snow, snow/sea ice and sea ice/ocean interfaces. DTC temperature sensors are spaced by 2 cm, with the top 20 cm representing the height above the air/snow interface. Red and orange boxes in (a) to (d) indicate WE1 and WE2 windows. Note the different temperature gradient scales for (e) and (f).



232 Figure 4: The upper 10 cm of the horizontally averaged density and SSA profiles of the snowpack over time derived from the SMP force
233 signals (where the average consists of 5 SMP profiles at each location), from (a & b) Snow 1 - A1, (c & d) Snow 1 - A5, and (e & f) Snow
234 2 - A2 locations. In each subplot, the horizontally averaged profile measured at the RSS measured on 4 November 2019 is illustrated for
235 comparison (blue dashed line). Map shows the immediate surroundings of the study site. The RSS is illustrated with a red dot, colored
236 lines show the extent of Snow1 and Snow2 sites, and SMP locations within these sites in colored shapes. The background is preliminary
237 quicklook-processed surface elevation data from the airborne laser scanner, where the whiter colors indicate high elevations of ≥ 2 m

238 During WE1, the air temperature increased from $\sim -32^{\circ}\text{C}$ (0800 UTC) to $\sim -16^{\circ}\text{C}$ (~ 2000 UTC) (Figure 3a). During WE2, air
239 temperature increased to $\sim -4^{\circ}\text{C}$ by ~ 1800 UTC and remained relatively warm until the end (Figure 3a). These changes clearly
240 influenced the temperature gradients across the snowpack, with a large, vertical temperature gradient of $> 7^{\circ}\text{C}/\text{cm}$ early in
241 WE1 decreasing to $\sim 3^{\circ}\text{C}/\text{cm}$ during WE2 (Figure 3f). Snow temperature gradients consistently exceeded $2.5^{\circ}\text{C}/\text{m}$, suggesting
242 temperature gradient-driven hoar metamorphism was occurring throughout the snowpack (e.g., Colbeck, 1989).

243
244 SMP-derived density and SSA profiles demonstrate an increase in density and decrease in SSA over time, in the uppermost (2
245 cm) snow layers (Figure 4). The density increase at Snow1 - A5 until 26 November is most distinct. The density and SSA
246 profile from the RSS measured on 4 November correlates well with those from Snow1 and Snow2, indicating representative
247 snowpack conditions between RSS and Snow1 and 2 locations. The average density change of the upper 2 cm between the last
248 and the first measurement at each location is $+30.7 \text{ kg/m}^3$ at Snow1 - A1, $+79.3 \text{ kg/m}^3$ at Snow1 - A5, and $+22.9 \text{ kg/m}^3$ at
249 Snow2 - A2 (Figure 4). The SSA change is -2.0 mm^{-1} at all snow pit locations (right panels).

250
251 The increase in surface snow density is typical for strong wind action on the snow (Lacroix et al., 2009; Savelyev et al., 2006).
252 Warmer air temperatures during the observed wind events, compared to pre-wind conditions (Figure 2) also increase the
253 likelihood for snow grains to sinter (e.g., Colbeck, 1989), favouring snow surface compaction. A SSA decrease indicates the
254 reduction in surface area, caused by rounding of snow grains, followed by sintering during wind transport (King et al., 2020).

255
256 **3.1.3 Snow Surface Topography Dynamics**

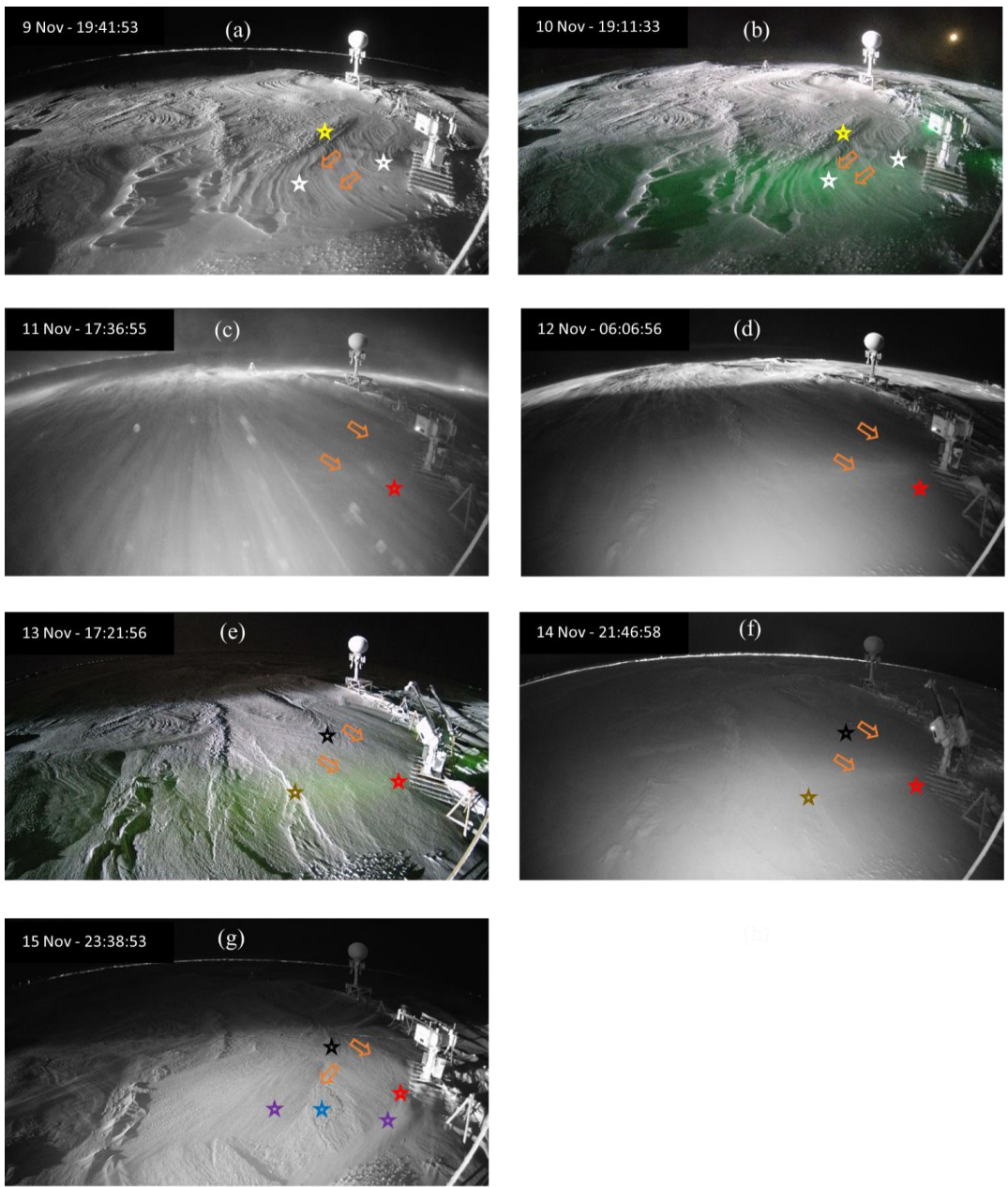
257 **3.1.3.1 Snow bedform evolution**

258 Wind events caused a dynamic evolution of snow bedforms in the radar scan area (Figure 5 and Supplemental Video 1). On 9
259 and 10 November (Figure 5a & b), the snow cover was characterised by bedform features (white stars), as well as crag and tail
260 features and patterned tail markings (yellow star), both typically found on relatively level sea ice (Filhol & Sturm, 2015). The
261 major axis of these bedforms is predominantly oriented parallel to the radar azimuthal scan direction.

262 Between 11 November until ~ 0800 UTC on 12 November, winds blew snow both radially and azimuthally relative to the
263 radar scan area at different times. Because the radar sled forms an aerodynamic obstacle, the snow drifted unevenly in the lee
264 of the sled (red star in Figure 5c-f and Supplemental Video 1). While snow depth could not be measured in the radar scan area,
265 considering the 30 cm radar sled height, snow drifts covering the edges of the sled indicate an increase in snow depth to > 30
266 cm directly in front of the radar. Blowing snow buried the existing bedforms from 9 and 10 November, creating a new drift
267 with its major axis oriented parallel to the azimuthal radar scans, and with an increasing slope (greater snow depth) with
268 increasing θ_{inc} (black star in Figure 5e-g). A new sastrugi also developed during WE1 (brown star in Figure 5e & f). WE2 on
269 15 November caused the rapid formation of two new snow drifts, oriented parallel to the prevailing wind direction (purple
270 stars in Figure 5g). A small pit-like feature also formed in the depression between the two drifts (dark blue star in Figure 5g),
271 while the drift (black star) that formed during WE1 is still visible.

272

273



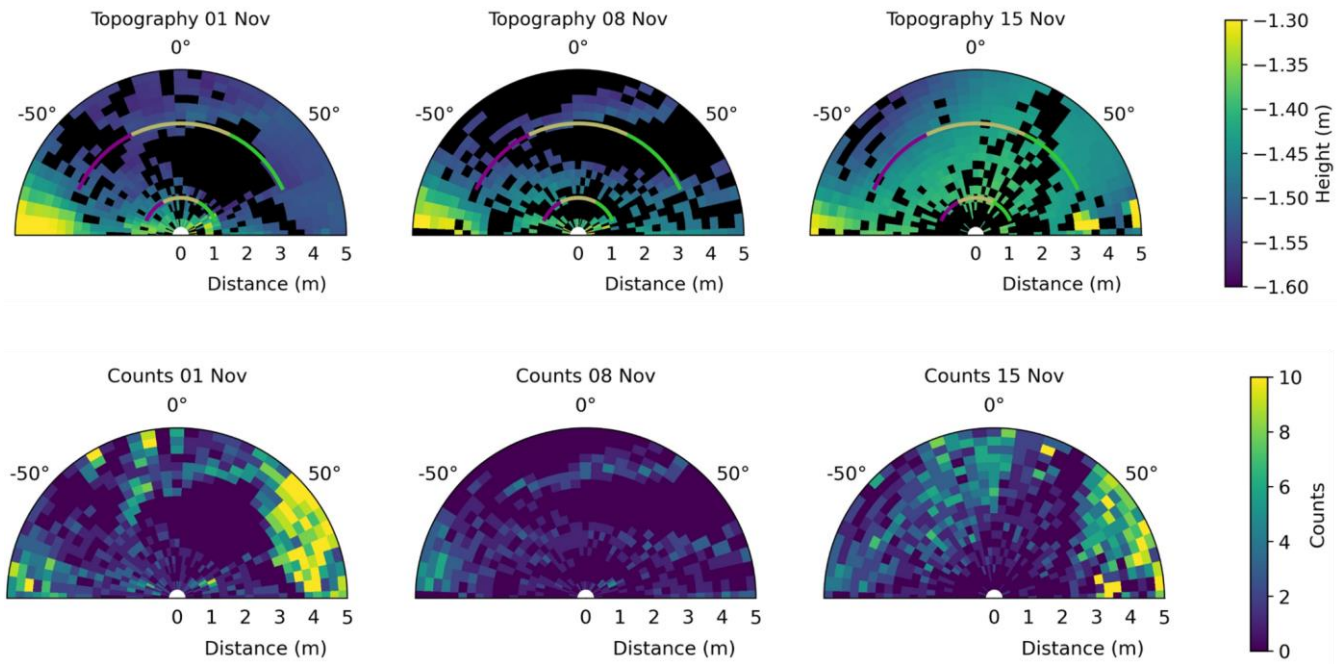
274

275 Figure 5: Images of the RSS scan area between (a) 9 November and (g) 15 November. Images were selected during times of the day when
 276 the ship's floodlight was illuminating the scanning area. The KuKa radar is on the far right on the images, while an L-band Scatterometer
 277 is on the upper right. Coloured stars represent major snow bedforms within the KuKa radar scan area, while orange arrows show the
 278 orientation of the bedforms in response to prevailing wind direction. All times are UTC.

279

3.1.3.2 Snow Surface Heights from TLS

280



281

282

Figure 6: TLS data (plan view) from 1, 8 and 15 November, from -90° to $+90^\circ$, where the angle indicates the azimuth of the radar positioner, and radial horizontal distance measured from the centre of the radar pedestal. The top panels show the topography as measured downwards (increasing negative) from the middle of the radar antenna arms. Black indicates no data recordings in that bin. Projections of the centres of the radar scan area are illustrated for 0° and 50° radar incidence angles between -65° to $+65^\circ$ azimuth range, superimposed on the TLS data in magenta and green for radar observations, respectively, and buff where the two overlap, as per Figure 1. The bottom panels indicate the number of TLS data points within each bin. Surface depressions resulting in 0 counts in the TLS data are due to obscuration by adjacent high areas due to snow/sea ice topography and human-made objects, as viewed from the TLS's oblique viewpoint some distance away.

289

The TLS-derived snow surface height data from 1, 8 and 15 November are illustrated in Figure 6 along with superimposed green, buff, and magenta lines, indicating the centres of the radar scan area. Data from 1 November are included for context (left panel), indicating that the surface topography was similar to 8 November (middle panel). The TLS data illustrate considerable surface height variability within the radar scan area between 8 and 15 November, with snow surface height increasing (middle and right panel), as also indicated by the raised snow drift (black star in Figure 5e-g) at approximately 0° to 45° azimuth in the CCTV images.

296 **3.2 Radar Waveforms**

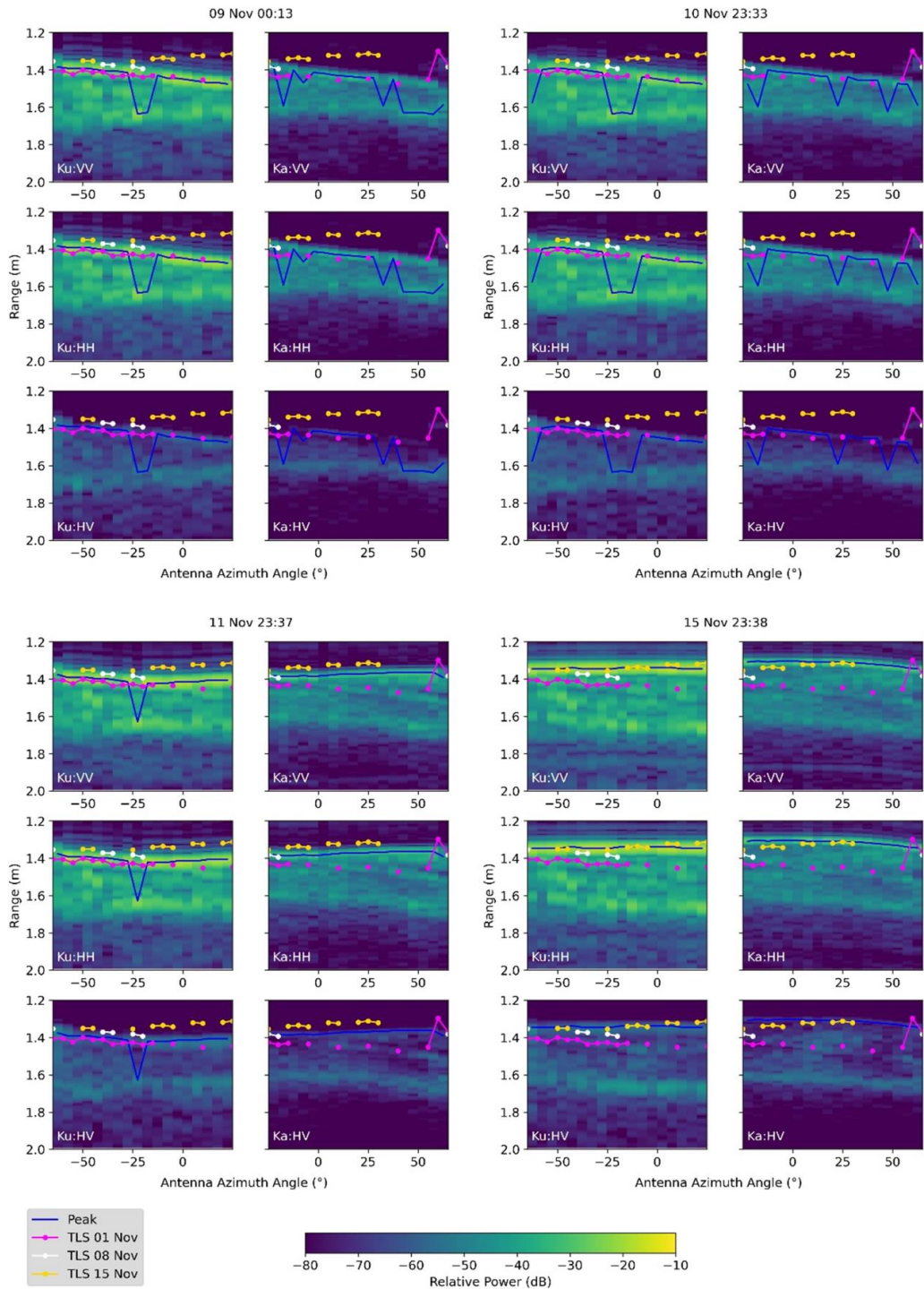
297 Figure 7 shows the temporal progression of Ka- and Ku-band radar waveforms at nadir, overlaid with spatially coincident
298 TLS-derived surface heights and averaged into individual 5° azimuth sectors. In the supplement, we provide an animation
299 (Supplemental Video 2) that includes all radar data from the two wind events, whereas here, we show four timeframes to
300 illustrate the radar response. As TLS data were acquired weekly, there are only these data available to overlay; in addition, as
301 relatively few data points were available for 8 November, we also show data from 1 November - before the wind events. TLS
302 data from all three dates are overlaid on all KuKa radar plots to demonstrate the time evolution of air/snow interface elevations
303 in the two datasets.

304

305 Prior to WE1, radar waveforms remained stable, with only small power variations over time. The peak power at VV and HH
306 generally corresponds to the air/snow interface in most θ_{az} bins, as also confirmed by the TLS-derived heights. A lower
307 scattering interface is also visible at ~ 20 to 40 cm below the air/snow interface, especially prominent in the HV data in both
308 frequencies, but also visible in the VV and HH data. The range values indicated in the radar waveforms are based on the speed
309 of light in free space. Correcting for a reduction of 80% for snow (Willatt et al., 2009), the lower interfaces lay ~ 16 to 32 cm
310 below the air/snow interface. To better understand this, we consider the HV waveform and local snow depth. Snow depth
311 measured behind the scan area during 4 and 14 November varied between 21 and 29 cm. Based on the very small amount of
312 radiation scattered from larger ranges, negligible penetration of Ku- and Ka-band signals into sea ice, and the consistency with
313 local snow depth, this interface in the HV data is very likely the snow/ice interface. A small amount of returned power is
314 expected from beyond due to snow and ice backscattering from the perimeter of the 30-50 cm radar scan area and sidelobes.

315

316

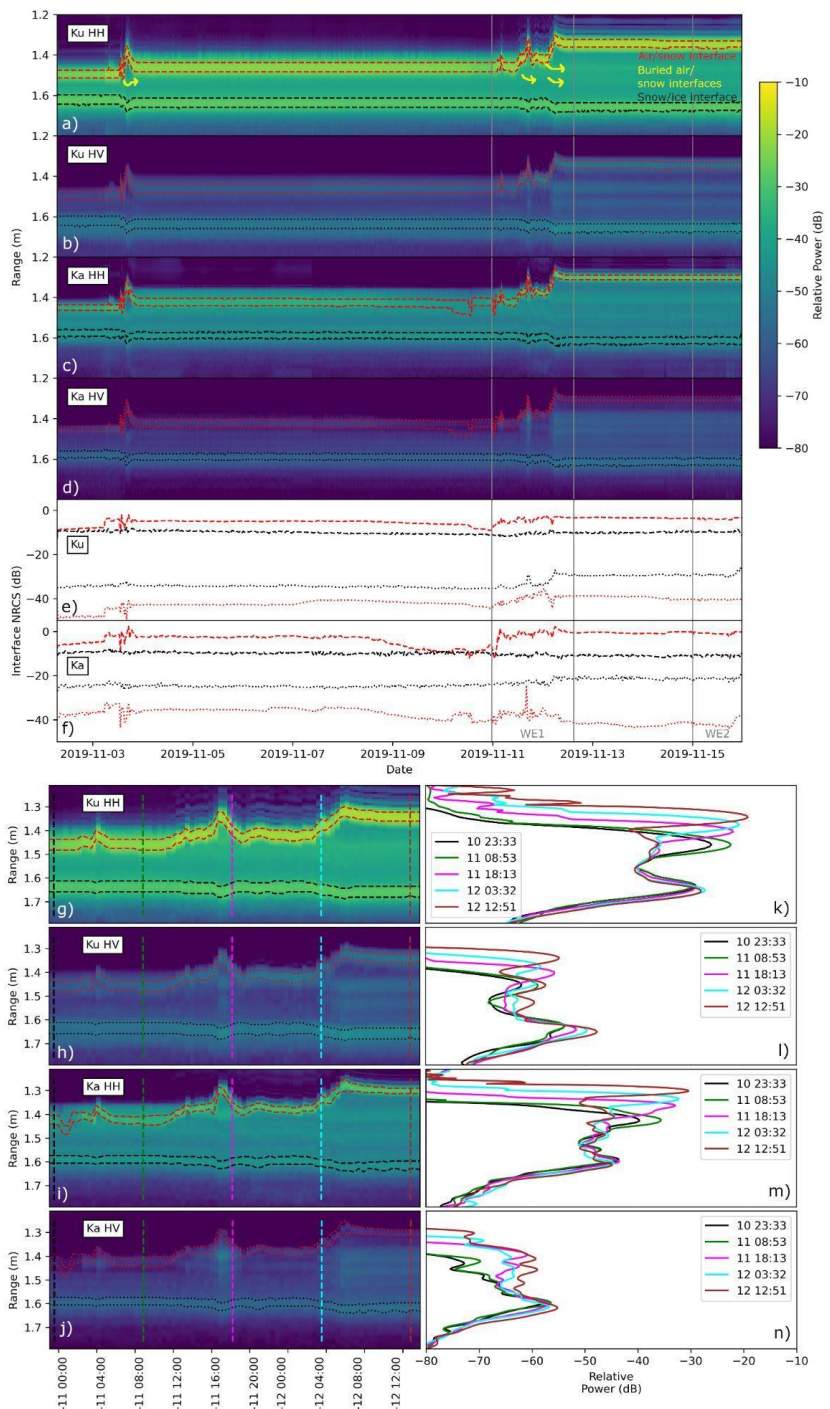


318 Figure 7: Progression of Ka- and Ku-band radar power-depth profiles at nadir between -65° to $+25^{\circ}$ (Ku-band) and -25° to $+65^{\circ}$ (Ka-band)
319 (azimuth ranges following Figure 1(e) and (f)). Range (y-axis) is given from the antenna phase centre, and the antenna azimuth angles (x-
320 axis) are the angles for that individual antenna. The highest power peak (averaged across all polarisations) is indicated with a blue line, and
321 the surface height in the spatially coincident TLS data is superimposed on top (coloured circles).

322 During WE1, radar waveforms at nadir show that the peak power at the air/snow interface shifted upwards due to snow
323 deposition at ~ 1800 UTC on 11 November (Figure 5c). This is followed by a snow scouring/erosion event, seen in the
324 downward movement of the peak power (Supplemental Video 2), followed by a second deposition event at approximately
325 0800 UTC on 12 November (Figure 5d) and upward movement of the peak power (Figure 8). It is interesting to note that the
326 Ka- and Ku-band scattering can still be seen from the previous air/snow interface on 9 and 10 November (yellow arrows on
327 Figure 8), as well as from the snow/ice interface, more prominent in the Ku-band. After WE1, the new air/snow interface
328 remains the dominant scattering surface for all polarizations and θ_{az} sectors.

329
330 During WE2, after accumulation of newly redistributed snow, the air/snow interface moved upwards to a closer range from
331 the antenna phase centre (bottom right panel in Figures 7 and 8). Scattering from the previously detected air/snow interface
332 (corresponding to the TLS data from 1 and 8 November) is still visible in both Ka- and Ku-band data (Figure 8). In addition,
333 the air/snow interface from 11 November remains visible in the Ka-band data in all polarisations (bottom left panel in Figure
334 7).

335
336 Next, we examined the highest amplitude peak at nadir, and how this varies with frequency and polarisation, through time.
337 Prior to WE1, the highest power peak originated from both air/snow and snow/ice interfaces at both frequencies (top panels in
338 Figure 7), suggesting variability in snow density (Figure 4) and surface topography (Figure 5) across the scan area. During and
339 after WE1 and WE2, the highest peak power remains almost always at the air/snow interface for both frequencies (bottom
340 panels in Figure 7). This means that the backscatter values in the following Figures 8 to 10 correspond to the air/snow or
341 snow/ice interfaces, depending on the θ_{az} sector and θ_{inc} , rather than a change in backscatter from one interface. The TLS
342 and radar waveforms also indicate a $\sim 2-5^{\circ}$ slope in the radar scan area especially at nadir (See Figures 6 and 7). Sloped
343 surfaces of $2-5^{\circ}$ will significantly affect the total backscatter amplitude. However, since surface scattering is the dominant
344 scattering mechanism at nadir, slightly sloped surfaces observed from the radar scan area likely do not affect the relative
345 distribution of scattering between the air/snow and the snow/ice interfaces.



349 Figure 8: Progression of the power-depth distributions over the commonly sampled area of the scan area between -25° and $+25^\circ \theta_{az}$. The
350 top panels a) - d) indicate the full time series from 2-15 November with the current air/snow and snow/ice interfaces indicated in red and
351 black, respectively. Sketched yellow arrows show how buried air/snow interfaces remain visible through time. Individual air/snow and
352 snow/sea ice interface NRCS values are determined by integrating power between the red/black dashed/dotted lines, which cover the range
353 bins where the power is within 2 dB from the air/snow and snow/sea ice interface peak. Time series of the interface NRCS values are
354 illustrated below the echograms (panels e and f). The timings of WE1 and WE2 are indicated with grey lines and labels across panels a) to
355 f). The bottom panels g) to j) show a temporal ‘zoom in’ of WE1. Panels k) to n) show line plots of the waveforms at the given times
356 corresponding to the vertical dashed lines on the echograms in g) to j).
357

358 Figure 8 illustrates the effect of WE1 and WE2 on HH-polarized waveform shapes and shows that the air/snow interface is
359 always the dominant scattering surface in both frequencies. In the HV data, the snow/ice interface is the dominant scattering
360 surface, but both interfaces are visible in both frequencies and all polarisations. Previous air/snow interfaces are also visible
361 as in Figure 7. The yellow arrows on the Ku-band HH plot show how the previous air/snow interfaces that remain visible when
362 additional snow accumulates. These buried interfaces, along with the snow/ice interface, appear at greater range when covered
363 with thicker snow due to the reduced wave propagation speed in snow relative to air, increasing the two-way travel time back
364 to the radar receiver.
365

366 For the Ka- and Ku-band HH data, there are relatively small changes to the NRCS associated with the snow/ice interface
367 (Figure 8e and f) and changes associated with the air/snow interface are much larger. Prior to WE1, the Ka-band air/snow
368 interface NRCS reduces from -5 to -10 dB before increasing during, and after WE1 to -3 dB. At Ku-band, a similar pattern is
369 observed with the air/snow NRCS reducing from -5 to -8 dB, then increasing to -3 dB following WE1. Most changes to NRCS
370 from wind events relate to backscatter changes from the air/snow interface. The Ka-band HV data show the air/snow interface
371 NRCS decreasing prior to WE1, increasing during the wind events and then reducing to a lower value than previously, while
372 the Ku-band data show the air/snow interface NRCS increasing during the wind events and remaining higher than previously.
373 The different behaviour at the two frequencies indicates that this could relate to roughness, i.e., the change in roughness is
374 dependent on length scales. This is illustrated by further detail in the waveform line plots which indicate how the waveform
375 shape changed with more variability relating to the air/snow interface and snow above the snow/ice interface in both
376 frequencies and polarisations. Both the Ka- and Ku-band HV show the snow/ice interface becoming brighter during the wind
377 events and remaining brighter afterwards; we speculate that this may be related to temperature-gradient driven metamorphism
378 of basal-snow.
379

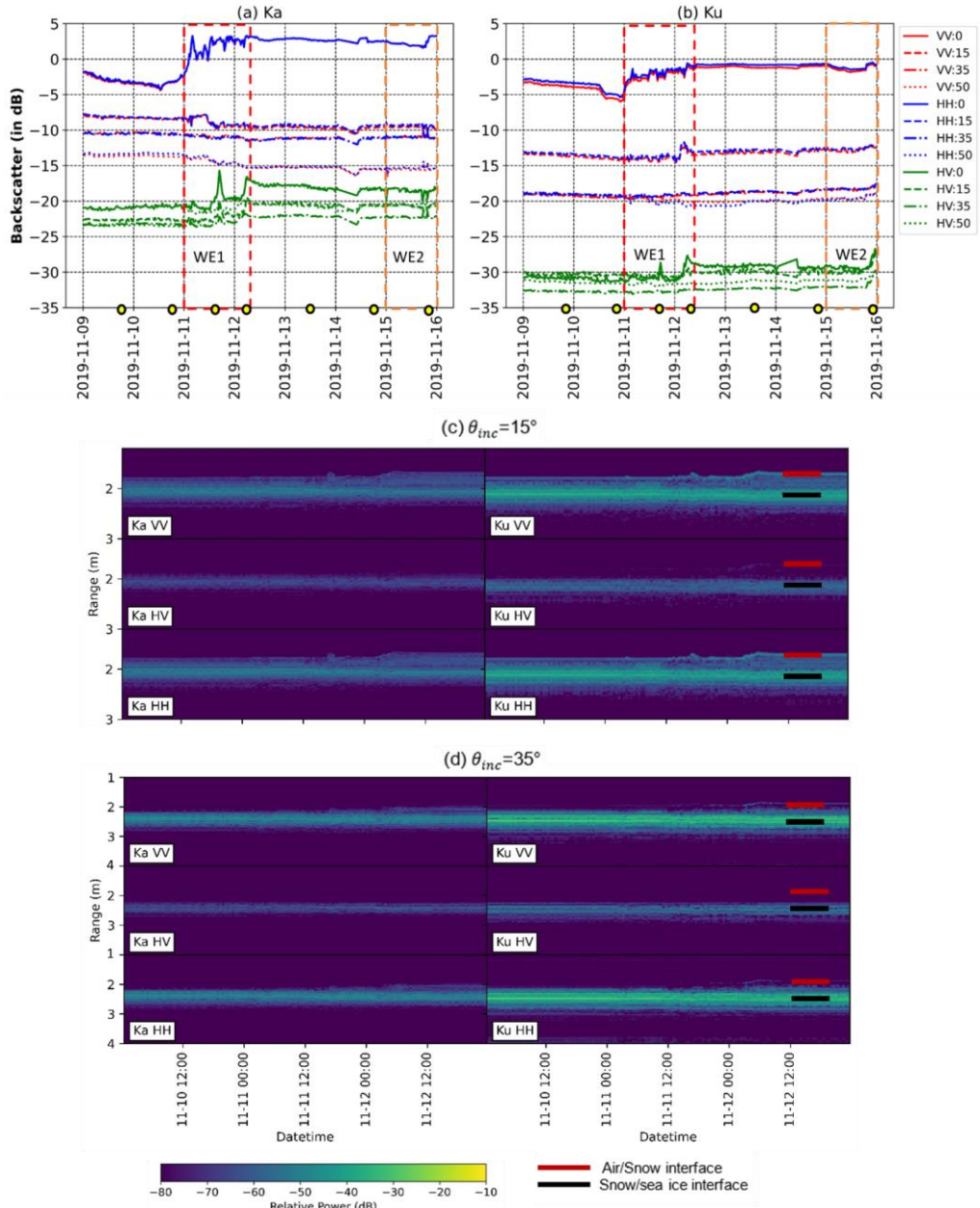
381 **3.3 Radar Backscatter**

382

383 This section focuses on the backscatter response from the overlapping area using azimuthally-averaged Ka- and Ku-band
384 backscatter time series at discrete $\theta_{inc} = 0^\circ, 15^\circ, 35^\circ$ and 50° . Included are radar echograms at $\theta_{inc} = 15^\circ$ and 35° during WE1,
385 to support backscatter interpretation. 2D interpolations of the spatial radar response along θ_{inc} and across $5^\circ \theta_{az}$ bins over both
386 Ka- and Ku-band scan area separately are also used to analyse backscatter changes at specific times on 9, 11 and 15 November.

387 **3.3.1 Azimuthally-averaged Backscatter**

388 During pre-wind conditions, both Ka- and Ku-band backscatter are relatively stable (Figure 9a & b). At nadir, VV and HH
389 returns primarily originate from the air/snow interface. With higher values of θ_{inc} , air/snow interface scattering decreases due
390 to the specular component of the backscattering not returning to the radar detector. The signal is therefore increasingly
391 dominated by snow volume scattering and incoherent surface scattering at the snow/sea ice interface. HV backscatter originates
392 primarily from the snow/sea ice interface (top panels in Figure 7).



393

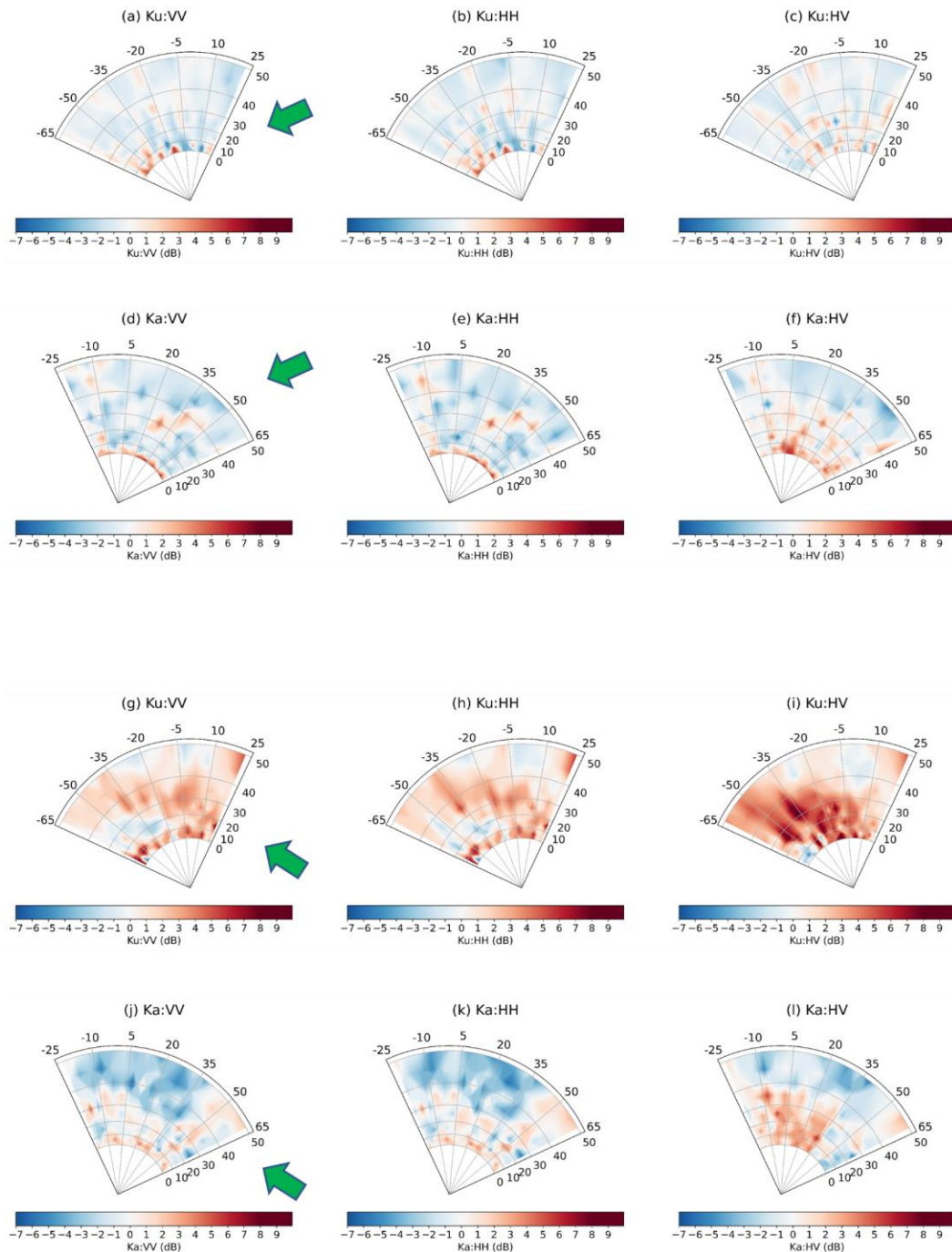
394 Figure 9: Azimuthally averaged (a) Ka- and (b) Ku-band backscatter at 0°, 15°, 35° and 50° incidence angles between 9 and 16 November,
395 from the overlapping -25° to +25° θ_{az} area. Red and orange indicate the WE1 and WE2 time window. Yellow circles correspond to times
396 of the day (in UTC) when the CCTV camera captured snapshots of radar scans. Panels (c) and (d) show time series of Ka- and Ku-band
397 radar echograms at (c) $\theta_{inc} = 15^\circ$ and (d) $\theta_{inc} = 35^\circ$ during WE1.

398 During WE1, nadir backscatter increases significantly, with a greater Ka-band increase of ~ 8 dB (VV and HH), compared to
399 a Ku-band increase of ~ 5 dB (VV and HH) (Figure 9a & b). The waveform analysis in Figures 7 and 8 indicates that the
400 amount of scattering from the snow/sea ice interface changed very little during WE1, while the scattering contribution to the
401 backscatter from the air/snow interface increased significantly due to increasing snow density (Figure 4) and decreasing radar-
402 scale roughness (Figure 5). This increase is accompanied by additional VV and HH backscatter from the previous, now-buried
403 air/snow interface (Figure 8). HV peak power shifts from the snow/sea ice interface to the air/snow interface and the buried
404 within-snow interface (Figure 8). This is clearly seen in the two significant HV increases at nadir, by up to 5 dB (Ka-band)
405 and by up to 4 dB (Ku-band) during WE1 (Figure 9a & b), coinciding with two short-term snow depositional events at ~ 1800
406 UTC on 11 November and around 0700 UTC on 12 November (Figure 5c & d and Supplemental Video 1).

407
408 At $\theta_{inc} = 15^\circ$ and 35° , the peak power interfaces during WE1 are much less obvious than at nadir but do exist (Figure 9c & d).
409 However, the bulk of the peak power moves from the air/snow interface to the snow/sea ice interface at all polarizations. The
410 shifting of peak power from the air/snow interface to the snow/sea ice interface coincides with a decrease in Ka-band VV and
411 HH backscatter by up to 2 dB at $\theta_{inc} = 15^\circ$ due to reduced air/snow interface roughness. The effect is less at $\theta_{inc} = 35^\circ$ due to
412 the snow volume scattering becoming more dominant compared to surface/interface scattering at the slanting cross section at
413 more oblique angles. The waveform analysis shows that the relative contribution of the snow/sea ice interface, snow volume
414 scattering and increased radar propagation delay due to increased snow accumulation becomes more important at shallow
415 angles (Leinss et al., 2014) and the air/snow interface becomes relatively less prominent due to lower surface roughness after
416 WE1. This feature is more observable in the HV data where the air/snow interface scattering is subtle, and the snow/sea ice
417 interface is brighter, with potential snow and ice volume scattering (middle panels in Figure 9c & d). Ku-band at non-nadir
418 incidence angles show negligible change in HV backscatter (more stable in HV at $\theta_{inc} = 35^\circ$ and 50°), compared to Ka-band
419 and pre-wind conditions (Figure 9b). It is expected that the HV backscatter is dominated by volume scattering processes and
420 that volume scattering is more prominent in Ka-band because of the shorter wavelength.

421
422 During WE2, Ka- and Ku-band backscatter at all θ_{inc} remains relatively stable (Figure 9a & b). Around ~ 2100 UTC on 15
423 November, a short-term snow depositional event (Supplemental Video 1) causes the Ka-band nadir backscatter to increase by
424 ~ 2 dB. The Ka-band waveform analysis shows scattering contributions from the air/snow interface during the snow deposition
425 and also from previously detected air/snow interface from 11 November (Figure 8 and lower right panels in Figure 7), causing
426 the additional 2 dB increase. Similar to WE1, Ku-band backscatter at $\theta_{inc} = 35^\circ$ and 50° remain nearly the same throughout
427 WE2 (Figure 9b). During WE2 it is likely that there is a slight snow surface roughness increase with a small nadir backscatter
428 decrease and a small off-nadir increase.

3.3.2 Change in Backscatter Response at $\Delta\theta_{az} = 5^\circ$



431 Figure 10: Polar plot panels (a) to (f) show the relative change in averaged Ku- and Ka-band backscatter at 5° azimuth sectors, as a
432 function of θ_{inc} , between WE1 and pre-wind conditions, acquired on 11 (WE1) and 9 November, at 2337 UTC and 0013 UTC,
433 respectively. Panels (g) to (l) show the same between windy conditions, acquired on 11 (WE1) and 15 (WE2) November, at 2337 UTC and
434 2338 UTC, respectively. Green arrows in (a) and (g) denote the prevailing wind direction on 11 and 15 November, respectively. The scan
435 times also correspond to yellow circles in Figure 9 and CCTV images in Figure 5a & c. Note: The 11 November CCTV image in Figure 5c
436 is acquired at 1736 UTC for image clarity showing blowing snow.

437 Changes in the spatial variation of the backscatter within each 5° θ_{az} sector acquired at specific date/times during pre-wind
438 conditions, WE1 and WE2 are shown in Figure 10. Compared to azimuthally-averaged Ka- and Ku-band backscatter (Figure
439 9), spatial variability in Ka- and Ku-band backscatter in response to wind events is evident at all polarizations and θ_{inc} . From
440 pre-wind conditions to WE1, the most striking feature is the development of a drifted snow dune directly in front of the sled
441 (red star in Figure 5) at $\theta_{inc} < 10^\circ$, which led to an increase in Ka- and Ku-band backscatter by up to 9 dB, at nadir throughout
442 all θ_{az} sectors. Beyond $\theta_{inc} = 10^\circ$, the change in Ka-band VV and HH backscatter are primarily negative, with spatially
443 heterogeneous areas of positive change, primarily in the θ_{az} sectors $> 20^\circ$ at $\theta_{inc} > 30^\circ$. The change in Ka-band HV backscatter
444 at $\theta_{inc} < 10^\circ$ is more consistently positive at θ_{az} sectors $< 0^\circ$, and it agrees well with the strong HV backscatter increase related
445 to deeper snow during the first snow depositional event that occurred halfway through WE1 on 11 November (Figure 5 and
446 Supplemental Video 1).

447

448 WE2 produces a stronger response in Ka- and Ku-band backscatter across the θ_{az} sectors, compared to WE1. Ka-band VV
449 and HH backscatter change is primarily negative (up to 7 dB) at $\theta_{inc} > 30^\circ$, while Ka- and Ku-band HV backscatter shows
450 strong positive change (up to 9.5 dB) at $\theta_{inc} > 40^\circ$. Images in Figure 5 and TLS scans from 8 and 15 November illustrate
451 changes in surface heights, due to the drifts that formed towards the left side of the KuKa radar (purple stars in Figure 5), and
452 the deeper snow appears to be captured by a strongly enhanced Ku-band HV response at θ_{az} sectors $< 0^\circ$. The large backscatter
453 changes along these sectors aligns with the wind direction also indicates change in snow topography from snow blowing
454 entrained from behind the radar.

455

456

457

458

459 **4. Discussion**460 **4.1 Impact of Snow Redistribution on Radar Signatures**

461 Our analyses demonstrate that Ka- and Ku-band backscatter and waveforms are sensitive to wind-induced snow redistribution.
462 During pre-wind conditions, the dominant radar scattering surface at nadir for both frequencies at the co-polarised channels
463 switches between the air/snow and snow/sea ice interfaces depending on local variations in snow surface density and
464 roughness. HV backscatter surface changes as a function of snow depth. This is illustrated by the waveform analysis, with the
465 range to the air/snow interface confirmed by georeferencing the radar and TLS data (Figures 7 and 8 and Supplementary Video
466 2), and the range to the snow/sea ice interface inferred from local snow depth measurements and the strong interface contrast
467 evident in backscatter in the radar waveforms and the opposite changes (increase/decrease) in the nadir and off-nadir
468 backscatter. Following WE1, the air/snow interface becomes the dominant scattering surface at nadir at all polarizations due
469 to the smoothening of the snow surface combined with the increased snow surface density. At satellite scales, this may
470 upwardly shift the retracked elevation and resulting sea ice freeboard retrievals by radar altimeters that assume the snow/sea
471 ice interface is the dominant scattering surface. This would introduce an overestimating bias on the sea ice thickness estimate;
472 however, a number of other uncertainties are also at play in this process, meaning this may move the retrieval closer or further
473 from the true value. Our surface-based findings are consistent with recent satellite-based work by Nab et al. (2023), who
474 showed a temporary lifting of CryoSat-2-derived radar freeboard in response to snow accumulation, but also higher wind
475 speeds and warmer air temperatures. Due to snow surface smoothening at non-nadir incidence angles, the relative scattering
476 contribution of the snow/sea ice interface compared to the air/snow interface increases, and the air/snow interface gradually
477 becomes invisible (Figure 9).

478 The Ku- and Ka-band radar backscatter is still sensitive to the presence of buried and historical air/snow interfaces within the
479 snowpack (Figures 7-9), which indicates that snow density and/or surface roughness contrasts (Figure 4) existing prior to wind
480 events continue to influence scattering even once additional snow is deposited (Figure 8). This is an important finding, because
481 even if an interface is not the dominant scattering surface, it can affect the waveform shape and assumptions about the surface
482 elevation retrieved from airborne and satellite radar altimetry data when there is no a priori information on the snow
483 geophysical history. In future studies, gathering TLS data on the snow surface roughness at high spatial (radar) and temporal
484 (e.g., daily or hourly) resolution would provide valuable information on the role of roughness. In addition, collecting near-
485 coincident measurements of snow density would provide information on the role of density affecting radar waveforms. We
486 would therefore recommend collecting these coincident datasets in future similar studies.

487

488 The relatively small backscatter observed from the snowpack at $\theta_{inc} = 15^\circ$ and 35° (Figure 9c & d) indicates dominant
489 scattering away from the radar. At these angles, most of the backscatter is associated with the snow/sea ice interface, and that
490 deeper snow is causing an increasing slant-range delay. The air/snow interface is directly impacted by the wind, experiencing

491 compaction to higher snow density and reduced surface roughness (Figures 4 and 5). The NRCS associated with the air/snow
492 interface increased by more than 5 dB during and following the wind events (Figure 8). Thus, utilising time-series backscatter
493 at both near- and off-nadir incidence angles may be useful for retrieving snow surface roughness and/or density changes,
494 though it may be difficult to separate these variables.

495
496 This study does not replicate airborne- and satellite-scale conditions (e.g., beam geometry, snow cover and ice type variability
497 on satellite-scales. Therefore, the waveform shape, return peak power and measured backscatter from the KuKa radar will be
498 different from airborne and satellite radar altimeters and scatterometers. Also of note is the highly localised nature of the radar
499 backscatter, which is a function of small-scale surface roughness combined with local θ_{inc} that includes some steep angles due
500 to snow drifts and bedforms in the scan area. Even at nadir viewing geometry, the beam-limited KuKa radar scan area covers
501 an angular range of 12–17° which is many orders of magnitude larger than the beamwidth of a satellite altimeter’s antenna and
502 two orders of magnitude larger than the equivalent-beamwidth of the altimeter’s pulse-limited footprint, which for CryoSat-2
503 is around 0.1° (Wingham et al., 2006).

504
505 The relative dominance of coherent over non-coherent backscatter mechanisms can vary significantly within the KuKa
506 beamwidth alone, with coherent reflections from near-specular surfaces dominating the radar response more easily at satellite
507 scales (Fetterer et al., 1992). However, even from a satellite viewing geometry, a smooth air/snow interface should produce
508 sufficient backscattering at Ku-band to modify the leading edge of the altimeter waveform response (Landy et al., 2019). The
509 larger satellite footprints may also include different surfaces, such as pressure ridges, rafting and rubble fields, hummocks,
510 refrozen leads, level first-year sea ice and open water. The effects of small scale roughness, larger scale topography and sub-
511 beamwidth θ_{inc} would combine in different ways for larger footprints, such as from satellites operating at large θ_{inc} , where
512 the distribution of local θ_{inc} may be less extreme and the signal would be dominated by the smooth parts of the surface (e.g.
513 Segal et al., 2020).

514
515 As mentioned earlier, the KuKa radar has a much higher vertical resolution than CryoSat-2 and AltiKa. This means that
516 although the individual interfaces would not be resolved in the satellite data, the waveform shape and hence retrieved elevation
517 could be affected by current, recent (days), and historical (weeks or longer) timescales of wind-driven redistribution changes
518 to the snow topography and physical properties. Retracking algorithms do not yet factor in the potential leftwards migration
519 (shortening range) of the waveform leading edge that could be caused by radar responses from the snow surface and historically
520 buried snow interfaces.

521 **4.2 The Azimuth Sectoring Approach and Interdependence of Wind and Snow Properties on Backscatter**

522 Azimuth sectoring provides an assessment of the backscatter heterogeneity across the radar scan area, here linked to the
523 dynamic evolution of snow bedforms during wind events. Our results show how sensitive the KuKa backscatter is to
524 development of snow bedforms and changing snow surface heights within the scan area with a directionality corresponding to
525 prevailing wind speed and direction.

526 The demonstrated influence of snowscape evolution from wind events prompts the need for further investigation of the relative
527 contributions of snow density, surface roughness and snow grain size on Ka- and Ku-band backscatter. There are three main
528 considerations: 1) measurement and parameterization of snow surface roughness on the scale of the radar wavelength are
529 poorly understood, especially with regard to temporal variability; 2) wind induces rapid density evolution at the snow surface
530 (Filhol & Sturm, 2015); and 3) strong covariance exists between snow density and snow temperature gradient metamorphosis
531 and snow grain size (Colbeck, 1989). Although there is no time series of density profiles available for the RSS, we show a
532 clear increase in density of the upper snowpack within profiles at comparable locations nearby the RSS (Figure 4). As a snow
533 surface densifies, surface scattering increases due to the enhanced dielectric contrast. Moreover, as snow warms, temperature-
534 gradient driven metamorphosis leads to density changes, which can also modify the roughness of surface and/or internal
535 interfaces, resulting in changes to backscatter (Lacroix et al., 2009).

536

537 The waveform analysis provides some insights on the effects of wind vs temperature. In a previous study, the significant
538 increase in C-band backscatter after a storm was attributed to enhanced radar-scale snow surface roughness and increasing
539 moisture content in snow with temperatures $> -6^{\circ}\text{C}$ (Komarov et al., 2017). Strong contributions from snow grain volume
540 scattering at C-band prior to the storm were masked by dominant surface scattering after wind roughening and mechanical
541 break-up of the snow grains during wind redistribution. In our study, the air and snow surface temperature did not reach -12°C
542 until late on 11 November (Figures 2 and 3), but the increasing wind speeds during WE1 (Figure 2) were already switching
543 the dominant scattering surface from being a mixture of the air/snow and snow/ice interface (prior to the wind events), to
544 almost exclusively the air/snow interface, and increasing the backscatter associated with the air/snow interface by ~ 5 dB
545 (Figure 8). The action of the wind on the snow surface dominated the change in the scattering surface. Therefore, we suggest
546 the effect of the wind on the snow roughness and/or on the snow density (wind compaction of the top layer) (Figure 4) causes
547 the air/snow interface to increasingly become the dominant scattering surface at Ka- and Ku-band frequencies.

548

549

550

551 **5. Conclusions**

552 This study details the impact of two wind events on surface-based Ka- and Ku-band radar signatures of snow on Arctic sea
553 ice, collected during the MOSAiC expedition in November 2019. The formation of snow bedforms and erosion events in the
554 radar scan area modified the snow surface heights, and this was recorded consistently by the radar instrument, a terrestrial laser
555 scanner and optical imagery. Analysis of radar waveforms demonstrated that the air/snow and snow/sea ice interfaces are
556 visible in both frequencies and all polarisations and incidence angles. During wind events, buried air/snow interfaces remain
557 clearly detectable at nadir, following new snow deposition. This shows that the historical conditions under which a snow cover
558 evolves, rather than only current conditions, affect backscatter.

559 We conclude that wind action and its effect on snow density and surface roughness, rather than temperature, which remained
560 $< -10^{\circ}\text{C}$ during the first recorded backscatter shifts, caused the observed change in the dominant scattering interface from a
561 mixture of air/snow and snow/sea ice interfaces, to predominantly the air/snow interface and nadir backscatter at the air/snow
562 interface increased by up to 5 dB. This effect would likely also be manifest in waveforms detected by satellite altimeters
563 operating at the same frequencies, e.g., AltiKa or CryoSat-2.

564 Compared to pre-wind conditions, nadir backscatter across the full radar azimuth increased by up to 8 dB (Ka-band) and by
565 up to 5 dB (Ku-band) during the wind events. This was caused by the formation of snow bedforms within the radar scan area,
566 which increased the snow surface roughness and/or density. Spatial variability in backscatter was evident across the radar scan
567 area, and that variability responded to the formation and evolution of snow bedforms, which in turn was driven by increasing
568 wind speeds and changing wind direction.

569 Overall, our results from the KuKa radar provide a process-scale understanding of how wind redistribution of snow on sea ice
570 can affect its topography and physical properties, and how these changes in turn can affect the radar properties of the snow
571 cover. Our results are relevant to both satellite altimetry and scatterometry through changes to radar waveforms and backscatter
572 during, and after wind events. However, more investigation is needed to deduce how much wind (i.e., conditions/thresholds
573 across space and time) is needed to impact satellite waveforms. Our findings cannot be applied directly to satellite instruments
574 without considering differences in footprint sizes, incidence angles, and the snow and sea ice properties sampled. However,
575 we do provide first-hand information on the frequency, incidence angle and polarisation responses of snow on sea ice, that are
576 important for modelling scattered radiation over an airborne and satellite footprint.

577 In future field-based experiments, we will aim to combine near-coincident KuKa radar data and snow depth measurements
578 (Stroeve et al., 2020), terrestrial laser scanner measurements of snow surface roughness and snow density profiles to better
579 characterise the effect of these variables on the radar range measurements. Forthcoming KuKa radar deployments on Antarctic
580 sea ice will produce further insights into snow geophysical processes (e.g. presence of slush, melt/refreeze layers, snow-ice

581 formation etc.) that may affect snow depth and sea ice thickness retrievals from satellite radar altimetry. In a windy Arctic
582 and the Antarctic, these methods will facilitate improved insights towards better quantifying the impact of snow redistribution
583 on accurate retrievals of snow/sea ice parameters from satellite radar missions such as SARAL/AltiKa, CryoSat2, Sentinel-
584 3A, Sentinel-6, SWOT, CRISTAL, and ScatSat-1.

585 **Code and Data availability:** Data used in this manuscript was produced as part of the international Multidisciplinary drifting
586 Observatory for the Study of the Arctic Climate (MOSAiC) with the tag MOSAiC20192020 and the Project ID: AWI PS122
587 00. KuKa radar data are available at <https://data.bas.ac.uk/full-record.php?id=GB/NERC/BAS/PDC/01486>. Meteorological
588 data collection was funded by National Science Foundation (#OPP-1724551).

589 **Video supplement.** Time-lapse video of wind events acquired by the CCTV camera (Supplemental Video 1) and animation of
590 radar+TLS waveforms during the wind events (Supplemental Video 2) are included in the Appendix.

591 **Author contributions.** VN processed the KuKa radar data and wrote the manuscript with input from co-authors. RW processed
592 and analyzed the KuKa radar waveforms including NRCS calculations of interfaces, overlaid TLS data on radar waveforms
593 and produced the radar+TLS time series animation. RM processed and plotted the DTC data. DCS processed the TLS data
594 from the raw format and wrote code for plotting and analysis of TLS data used in this paper. AJ produced the floe map for the
595 paper. DW and DK processed the SMP data and DW produced the SMP plot. JS, RS, TG and JL provided extensive inputs
596 and reviews to the paper. RT, JY, TN, DJ, MH, JM, GS, SH, RR, MT, MM, MS, DW, MG, CD, IR, CP, IM, and MH provided
597 valuable editorial comments. Many co-authors helped collect data during MOSAiC.

598 **Competing Interests:** None

599 **Acknowledgements.** This work was carried out as part of the international Multidisciplinary drifting Observatory for the Study
600 of the Arctic Climate (MOSAiC), MOSAiC20192020 and was funded to JS in part by the Canada 150 Chair program
601 (#G00321321), the National Science Foundation (NSF) Grant #ICER 1928230, and the Natural Environment Research Council
602 (NERC) Grants #NE/S002510/1 (also funded RW), and #NE/L002485/1. Funding was also provided to JS by the European
603 Space Agency (grant no. PO #5001027396). This project has received funding from the European Union’s Horizon 2020
604 research and innovation programme (# 01003826). VN was additionally supported by Canada’s Marine Environmental
605 Observation, Prediction and Response Network (MEOPAR) postdoctoral funds. MG was supported by the DOE Atmospheric
606 System Research Program (#DE-SC0019251, #DE-SC0021341). GS, MH, AJ and SH were supported by the the German
607 Ministry for Education and Research (BMBF) through the MOSAiC IceSense projects (#03F0866B to GS and MH;
608 #03F0866A to AJ and SH) and by the Deutsche Forschungsgemeinschaft (DFG) through the International Research Training
609 Group IRTG 1904 ArcTrain (#221211316). MS and DW were supported by the European Union’s Horizon 2020 research and
610 ARICE (#730965) for MOSAiC berth fees associated with the DEARice participation; and to Swiss Polar Institute grant

611 SnowMOSAiC (#EXF–2018–003). CD was funded through the EUMETSAT MOSAiC project (#4500019119). We thank all
612 scientific personnel and crew members involved in the expedition of the Research Vessel Polarstern during MOSAiC in 2019–
613 2020 (AWI_PS122_00) and Thomas Johnson (University College London) for advising on plots and animations.

614 **References**

615 Armitage, T. W., and Kwok, R. (2021). SWOT and the ice-covered polar oceans: An exploratory analysis. *Advances in Space*
616 *Research*, 68(2), 829-842, <https://doi.org/10.1016/j.asr.2019.07.006>.

617 Armitage, T. W., & Ridout, A. L. (2015). Arctic sea ice freeboard from AltiKa and comparison with CryoSat-2 and Operation
618 IceBridge. *Geophysical Research Letters*, 42(16), 6724-6731, <https://doi.org/10.1002/2015GL064823>.

619 Clemens-Sewall, D., Parno, M., Perovich, D., Polashenski, C., & Raphael, I. A. (2022). FlakeOut: A geometric approach to
620 remove wind-blown snow from terrestrial laser scans. *Cold Regions Science and Technology*, 201, 103611,
621 <https://doi.org/10.1016/j.coldregions.2022.103611>

622 Colbeck, S. C. (1989). Snow-crystal growth with varying surface temperatures and radiation penetration. *Journal of*
623 *Glaciology*, 35(119), 23-29, <https://doi.org/10.3189/002214389793701536>

624 Cox, C., Gallagher, M., Shupe, M., Persson, O., & Solomon, A. (2021). 10-meter (m) meteorological flux tower measurements
625 (Level 1 Raw), Multidisciplinary Drifting Observatory for the Study of Arctic Climate (MOSAiC), central Arctic, October
626 2019 - September 2020. *Arctic Data Center*. <https://doi.org/10.18739/A2VM42Z5F>

627 Doviak, R. J., & Zrnić, D (1984). Doppler Radar and Weather Observations. Academic Press, 458 pp.

628 Filhol, S., & Sturm, M. (2015). Snow bedforms: A review, new data, and a formation model. *Journal of Geophysical Research:*
629 *Earth Surface*, 120(9), 1645-1669, <https://doi.org/10.1002/2015JF003529>.

630 Fetterer, F. M., Drinkwater, M. R., Jezek, K. C., Laxon, S. W., Onstott, R. G., & Ulander, L. M. (1992). Sea ice altimetry.
631 Washington DC *American Geophysical Union Geophysical Monograph Series*, 68, 111-135.

632 Guerreiro, K., Fleury, S., Zakhrova, E., Rémy, F., & Kouraev, A. (2016). Potential for estimation of snow depth on Arctic
633 sea ice from CryoSat-2 and SARAL/AltiKa missions. *Remote Sensing of Environment*, 186, 339-349,
634 <https://doi.org/10.1016/j.rse.2016.07.013>.

635 Iacozza, J., & Barber, D. G. (2010). An examination of snow redistribution over smooth land-fast sea ice. *Hydrological*
636 *Processes* 24(7), 850-865, <https://doi.org/10.1002/hyp.7526>.

637 Johnson, J. B., & Schneebeli, M. (1999). Characterizing the microstructural and micromechanical properties of snow. *Cold*
638 *Regions Science and Technology*, 30(1-3), 91-100, [https://doi.org/10.1016/S0165-232X\(99\)00013-0](https://doi.org/10.1016/S0165-232X(99)00013-0).

639 Komarov, A. S., Landy, J. C., Komarov, S. A., & Barber, D. G. (2017). Evaluating scattering contributions to C-band radar
640 backscatter from snow-covered first-year sea ice at the winter–spring transition through measurement and modeling. *IEEE*
641 *Transactions on Geoscience and Remote Sensing*, 55(10), 5702-5718, <https://doi.org/10.1109/TGRS.2017.2712519>.

642 Kurtz, N. T., & Farrell, S. L. (2011). Large-scale surveys of snow depth on Arctic sea ice from Operation IceBridge.
643 *Geophysical Research Letters*, 38(20), <https://doi.org/10.1029/2011GL049216>.

644 Kern, M., Cullen, R., Berruti, B., Bouffard, J., Casal, T., Drinkwater, M. R., ... & Yackel, J. (2020). The Copernicus Polar Ice
645 and Snow Topography Altimeter (CRISTAL) high-priority candidate mission. *The Cryosphere*, 14(7), 2235-2251,
646 <https://doi.org/10.5194/tc-14-2235-2020>.

647 King, J., Howell, S., Brady, M., Toose, P., Derksen, C., Haas, C., & Beckers, J. (2020). Local-scale variability of snow density
648 on Arctic sea ice. *The Cryosphere*, 14(12), 4323-4339, <https://doi.org/10.5194/tc-14-4323-2020>.

649 Landy, J. C., Tsamados, M., & Scharien, R. K. (2019). A facet-based numerical model for simulating SAR altimeter echoes
650 from heterogeneous sea ice surfaces. *IEEE Transactions on Geoscience and Remote Sensing*, 57(7), 4164-4180,
651 <https://doi.org/10.1109/TGRS.2018.2889763>.

652 Leinss, S., Lemmetyinen, J., Wiesmann, A., & Hajnsek, I. (2014, June). Snow Structure Evolution Measured by Ground Based
653 Polarimetric Phase Differences. In EUSAR 2014; 10th European Conference on Synthetic Aperture Radar (pp. 1-4). VDE.

654 Löwe, H., Egli, L., Bartlett, S., Guala, M., and Manes, C. (2007), On the evolution of the snow surface during snowfall,
655 *Geophys. Res. Lett.*, 34, L21507, <https://doi.org/10.1029/2007GL031637>.

656 Lacroix, P., Legresy, B., Remy, F., Blarel, F., Picard, G., & Brucker, L. (2009). Rapid change of snow surface properties at
657 Vostok, East Antarctica, revealed by altimetry and radiometry. *Remote Sensing of Environment*, 113(12), 2633-2641,
658 <https://doi.org/10.1016/j.rse.2009.07.019>.

659 Lawrence, I. R., Tsamados, M. C., Stroeve, J. C., Armitage, T. W., & Ridout, A. L. (2018). Estimating snow depth over Arctic
660 sea ice from calibrated dual-frequency radar freeboards. *The Cryosphere*, 12(11), 3551-3564, <https://doi.org/10.5194/tc-12-3551-2018>.

661 Lawrence, I. R., Armitage, T. W., Tsamados, M. C., Stroeve, J. C., Dinardo, S., Ridout, A. L., ... & Shepherd, A. (2021).
662 Extending the Arctic sea ice freeboard and sea level record with the Sentinel-3 radar altimeters. *Advances in Space Research*,
663 68(2), 711-723, <https://doi.org/10.1016/j.asr.2019.10.011>.

664 Moon, W., Nandan, V., Scharien, R. K., Wilkinson, J., Yackel, J. J., Barrett, A., ... & Else, B. (2019). Physical length scales
665 of wind-blown snow redistribution and accumulation on relatively smooth Arctic first-year sea ice. *Environmental Research
666 Letters*, 14(10), 104003, <https://doi.org/10.1088/1748-9326/ab3b8d>

667 Nab, C., Mallett, R., Gregory, W., Landy, J., Lawrence, I., Willatt, R., ... & Tsamados, M. (2023). Synoptic variability in
668 satellite altimeter-derived radar freeboard of Arctic sea ice. *Geophysical Research Letters*, e2022GL100696,
669 <https://doi.org/10.1029/2022GL100696>

670 Nandan, V., Scharien, R., Geldsetzer, T., Mahmud, M., Yackel, J. J., Islam, T., ... & Duguay, C. (2017). Geophysical and
671 atmospheric controls on Ku-, X-and C-band backscatter evolution from a saline snow cover on first-year sea ice from late-
672 winter to pre-early melt. *Remote Sensing of Environment*, 198, 425-441, <https://doi.org/10.1016/j.rse.2017.06.029>

674 Nicolaus, M., Perovich, D. K., Spreen, G., Granskog, M. A., von Albedyll, L., Angelopoulos, M., ... & Wendisch, M. (2022).
675 Overview of the MOSAiC expedition: Snow and sea ice. *Elem Sci Anth*, 10(1), 000046,
676 <https://doi.org/10.1525/elementa.2021.000046>.

677 Proksch, M., Löwe, H., & Schneebeli, M. (2015). Density, specific surface area, and correlation length of snow measured by
678 high-resolution penetrometry. *Journal of Geophysical Research: Earth Surface*, 120(2), 346-362,
679 <https://doi.org/10.1002/2014JF003266>.

680 Segal, R. A., Scharien, R. K., Cafarella, S., & Tedstone, A. (2020). Characterizing winter landfast sea-ice surface roughness
681 in the Canadian Arctic Archipelago using Sentinel-1 synthetic aperture radar and the Multi-angle Imaging SpectroRadiometer.
682 *Annals of Glaciology*, 61(83), 284-298, <https://doi.org/10.1017/aog.2020.48>.

683 Saveliev, S. A., Gordon, M., Hanesiak, J., Papakyriakou, T., & Taylor, P. A. (2006). Blowing snow studies in the Canadian
684 Arctic shelf exchange study, 2003–04. *Hydrological Processes*, 20(4), 817-827, <https://doi.org/10.1002/hyp.6118>.

685 Stroeve, J., Nandan, V., Willatt, R., Tonboe, R., Hendricks, S., Ricker, R., ... & Tsamados, M. (2020). Surface-based Ku-and
686 Ka-band polarimetric radar for sea ice studies. *The Cryosphere*, 14(12), 4405-4426, <https://doi.org/10.5194/tc-14-4405-2020>.

687 Singh, U. S., & Singh, R. K. (2020). Application of maximum-likelihood classification for segregation between Arctic multi-
688 year ice and first-year ice using SCATSAT-1 data. *Remote Sensing Applications: Society and Environment*, 100310,
689 <https://doi.org/10.1016/j.rsase.2020.100310>.

690 Spreen, Gunnar; Huntemann, Marcus; Thielke, Linda; Naderpour, Reza; Mahmud, Mallik; Tavri, Aikaterini (2022): Infrared
691 camera raw data (ir_variocam_01) at the remote sensing site on the ice floe during MOSAiC expedition 2019/2020.
692 PANGAEA, <https://doi.org/10.1594/PANGAEA.940717>

693 Spreen, Gunnar; Huntemann, Marcus; Naderpour, Reza; Mahmud, Mallik; Tavri, Aikaterini; Thielke, Linda (2021): Optical
694 IP Camera images (VIS_INFRALAN_01) at the remote sensing site on the ice floe during MOSAiC expedition 2019/2020.
695 PANGAEA, <https://doi.org/10.1594/PANGAEA.939362>

696 Trujillo, E., Leonard, K., Maksym, T., and Lehning, M. (2016), Changes in snow distribution and surface topography following
697 a snowstorm on Antarctic sea ice, *J. Geophys. Res. Earth Surf.*, 121, 2172– 2191, <https://doi.org/10.1002/2016JF003893>.

698 Tilling, R. L., Ridout, A., & Shepherd, A. (2018). Estimating Arctic sea ice thickness and volume using CryoSat-2 radar
699 altimeter data. *Advances in Space Research*, 62(6), 1203-1225, <https://doi.org/10.1016/j.asr.2017.10.051>.

700 Ulaby, F. T., Held, D., Dodson, M. C., McDonald, K. C., & Senior, T. B. (1987). Relating polarization phase difference of
701 SAR signals to scene properties. *IEEE Transactions on Geoscience and Remote Sensing*, (1), 83-92,
702 <https://doi.org/10.1109/TGRS.1987.289784>.

703 Ulaby, F. T., Long, D. G., Blackwell, W. J., Elachi, C., Fung, A. K., Ruf, C., ... & Van Zyl, J. (2014). *Microwave radar and
704 radiometric remote sensing* (Vol. 4, No. 5, p. 6). Ann Arbor, MI, USA: University of Michigan Press.

705 Virtanen, P., Gommers, R., Oliphant, T. E., Haberland, M., Reddy, T., Cournapeau, D., ... & Van Mulbregt, P. (2020). SciPy
706 1.0: fundamental algorithms for scientific computing in Python. *Nature methods*, 17(3), 261-272,
707 <https://doi.org/10.1038/s41592-019-0686-2>.

708 Willatt, R. C., Giles, K. A., Laxon, S. W., Stone-Drake, L., & Worby, A. P. (2009). Field investigations of Ku-band radar
709 penetration into snow cover on Antarctic sea ice. *IEEE Transactions on Geoscience and remote sensing*, 48(1), 365-372,
710 <https://doi.org/10.1109/TGRS.2009.2028237>.

711 Wingham, D. J., Francis, C. R., Baker, S., Bouzinac, C., Brockley, D., Cullen, R., ... & Wallis, D. W. (2006). CryoSat: A
712 mission to determine the fluctuations in Earth's land and marine ice fields. *Advances in Space Research*, 37(4), 841-871,
713 <https://doi.org/10.1016/j.asr.2005.07.027>.

714 Wagner, D. N., Shupe, M. D., Cox, C., Persson, O. G., Uttal, T., Frey, M. M., ... & Lehning, M. (2022). Snowfall and snow
715 accumulation during the MOSAiC winter and spring seasons. *The Cryosphere*, 16(6), 2373-2402, <https://doi.org/10.5194/tc-16-2373-2022>.

717 Yackel, J. J., & Barber, D. G. (2007). Observations of snow water equivalent change on landfast first-year sea ice in winter
718 using synthetic aperture radar data. *IEEE Transactions on Geoscience and Remote Sensing*, 45(4), 1005-1015,
719 <https://doi.org/10.1109/TGRS.2006.890418>.